Experimental and numerical investigation of a freefall wedge vertically entering the water surface

Jingbo Wang[a,*], Claudio Lugni[b,a], Odd Magnus Faltinsen[a]

[a]*Centre for Autonomous Marine Operations and Systems (AMOS), Norwegian University of Science and Technology, N-7491 Trondheim, Norway*

[b]*CNR-INSEAN: Italian Research Council - Institute for Marine Technology, Roma, Italy*

Abstract

Experiments and numerical methods are developed to investigate the water entry of a freefall wedge with a focus on the evolution of the pressure on the impact sides (the side contacting water) and the top side (the dry side on the top of the wedge), evolution of the global hydrodynamic loads, evolution of the air-water interface, and wedge motion. It is found that a typical water entry of a freefall wedge can be divided into slamming, transition, collapse and post-closure stages. A single-fluid numerical model is presented to simulate the first three stages. The results are compared to experiments and good agreements are obtained. A two-fluid BEM is proposed to investigate the influence of the air flow before the closure of the cavity created on the top of the wedge. It is found that for the closure of the 2D cavity, the air flow starts to play an important role just before closure but due to the short duration, the influence of air flow on the body velocity and configuration of the air-water interface is limited.

Keywords: *wedge; water entry; free surface; loads; cavity; two-fluid BEM*

1. Introduction

Lifeboats are widely used in ships and offshore platforms to rescue humans in emergency conditions. When a freefall lifeboat enters water, the fore part with a wedge-shaped cross section may impact the water surface at high speed. The impact between the lifeboat and the water results in impulsive pressures on the hull and large accelerations of the boat (the absolute value of the acceleration can reach and even exceed 10 g). These loads can damage the lifeboat and/or injure occupants. After the water reaches the knuckle line of the lifeboat, flow separation occurs and a cavity is formed on the top of the lifeboat. This significantly influences the transient hydrodynamic forces acting on the lifeboat so that it experiences a significant drop in acceleration. Eventually, the cavity is closed at the stern of lifeboat. After the closure, the compressibility of the air entrapped in the cavity matters. It is associated with the oscillation of the cavity pressure, which leads to the oscillation of the longitudinal acceleration of the lifeboat. Good understanding of these phenomena is vitally important for the effective design of lifeboats, motivating the present investigation of the water entry of a freefall wedge.

Experiments and numerical methods are developed with a focus on the: pressure evolution on the impact and top sides of the wedge, evolution of the global hydrodynamic loads, evolution of the air-water interface (cavity) and wedge motions. In addition, the influence of the air flow before the closure of the cavity is investigated. Experiments and numerical simulations showed that a freefall wedge entering a free surface of water may experience four successive stages:

Slamming stage. At the beginning of the impact, the water rises up and jets are formed at the body sides. Before the water reaches the knuckle of the wedge and flow separation occurs, the slamming

* Corresponding author. Tel: +47 95978375. E-mail address: jingbo.wang@hotmail.com

force acting on the body rapidly increases due to the rapid change of the added mass of the wedge. The flat-plate approximation of the added mass, i.e. $A_{33} = 0.5\rho\pi c^2$, shows that it grows quadratically with respect to the half wetted breadth c. By assuming a constant entry speed and neglecting the effect of the gravity, the slamming force/pressure and the free surface profile have been widely studied [1-8]. Under the influence of the slamming force, the freefall wedge experiences a rapid change of vertical acceleration.

Transition stage. When the jet reaches the knuckle of the wedge, non-viscous flow separation occurs. The jet breaks up into spray. After the root of the jet/spray leaves the knuckle of the wedge, the rate of change of the added mass reduces and this leads to the strong drop in the slamming force which corresponds to the significant drop in the acceleration. The transition stage starts when the root of the spray leaves the knuckle and it ends when it is far away from the knuckle (approximately after the top side of the wedge reaches the still water level).

Collapse stage. After the transition stage, an open cavity is formed on the top of the wedge [9].The open cavity expands laterally at the beginning. The hydrostatic term in the Bernoulli's equation resists the expansion of the cavity causing its contraction and pinch-off (closure). During this stage, the hydrodynamic loads change slowly.

Post-closure stage. When the cavity is closed, the air compressibility plays an important role and leads to an oscillation of the cavity pressure, of the hydrodynamic loads and of the wedge acceleration. We also call this stage an 'oscillation stage'.

In this paper, the first three stages are studied in deep. We develop experimental and numerical methods to investigate the physical phenomena involved during the water entry of a freefall wedge. The experimental and numerical methods are verified by comparing the results, and used to investigate the influence of the air flow before the pinch-off of the cavity. In the companion paper [10], we discuss the mechanics behind the physical phenomena during the water entry of freefall wedges.

2. Experiments

Experiments are conducted to understand the physical behavior of the phenomena connected with the vertical motion of the wedge and the cavity dynamics during a freefall wedge entering the water surface. The main goals of the experiments are to investigate the: evolution of the pressure along the impact sides and the top side of the wedge, evolution of the global hydrodynamic loads, evolution of the air-water interface, and vertical motion of the wedge. The experimental results are also used to verify/validate the numerical models developed.

2.1 Experimental setup

An *ad hoc* experimental apparatus has been designed at CNR-INSEAN for the experimental tests. It consists of a wedge cylinder, a water tank and driving and releasing mechanisms. A global sketch of the water tank and the driving mechanism is shown in Fig. 1 (lateral view) and Fig. 2 (front view).

Tank. A tank has been designed for proper measurements of the flow around the body. In order to assure the complete visibility of the flow field as well as of the free surface deformation, the wall and the bottom of the tank have been built by using plates of Plexiglas with thickness 40 mm. The main dimensions of the tank are reported in Figs. 1-2. The tank length is 3 m to avoid interaction between the hydrodynamic field and the ends of the tank. The tank width is 400 mm which is sufficient to avoid 3D effects from the ends of the cylinder (due to the presence of gaps between the ends of the cylinder and the tank walls) affecting the central cross section of the cylinder where measurements are taken. A

water depth H=1000~1200 mm has been used, corresponding to a ratio h_0/H = 0.04~0.048, with h_0 the height of wedge prism. A structure fixed to the floor (element 6 on the sketch of Fig. 1) supports the wall of the tank and keeps its bottom at a distance of 300 mm from the floor to allow for lighting from below.

Driving and releasing mechanisms. The wedge cylinder (element 4 in Fig. 1) is connected to the sliding beam (element 9 in Fig. 1). They are free to fall from a height h. During the fall, the sliding beam moves along two vertical linear guides (element 7 in Fig. 1) screwed on a steel structure (element 1 in the Fig. 1), which is rigidly fixed to the ceiling of the lab. This structure is also used as support for the system pulley-cable and electric magnet release mechanism (elements 2+3+8 in Fig. 1). At the initial time instant, the electric magnet is switched off and the cylinder falls, attaining a theoretical impact speed of $\sqrt{2gh}$.

Wedge cylinder. The wedge cylinder consists of a wedge prism and three orthogonal plates as shown in Fig. 3. The two impact sides and the top side (hatch) of the wedge prism are made from 5 mm aluminum plates. Screws are used to connect the impact sides and the hatch. The orthogonal plates are made from 6 mm aluminum plates, which are welded on the hatch. The nominal dimensions of the wedge prism are 48 mm high, 166 mm wide and 396 mm long, which results in a deadrise angle of 30° and the length/width ratio of 2.4. We note that a larger cross-section leads to a small length/width ratio (3D effects matters) and small Froude numbers (not as desired), while a smaller cross-section leads to an inner space that is insufficient to mount pressure transducers and weak bending stiffness (hydroelasticity may matter during impact).

The maximum Froude number $Fn = V_0/\sqrt{gc_0}$ with V_0 the initial entry speed, g the acceleration of gravity and c_0 the half width of the wedge is limited by the maximum falling height of wedge, which is approximately 2.5 m in the used experimental facility.

The arrangement of the wedge prism and the description of the pressure probes are shown in Fig. 4. Four stiffeners are built inside the wedge prism and screw holes are made on the stiffeners. A bigger stiffener is built in the center of the wedge prism. Three pressure transducers (Kulite XCQ-62) are placed on the hatch of the wedge and other three (Kulite XT190) are placed on the impact side. The sensitive part of the probe is a flat disc with diameter around 4 mm for the XT190 and 1 mm for the XCQ-62. An exit hole is made on the hatch and a waterproof tube is connected on the hole to guide the cables of transducers out from the wedge prism.

The wedge cylinder is connected to the sliding beam (element 9 in Fig. 1) by two connecting cylinders, as illustrated in Fig. 1. The equivalent mass of the wedge cylinder, that is the sum of the sliding beam, the connecting cylinders, the orthogonal plates and the wedge prism, is 12.8 kg (which leads to 32.3 kg/m).

Camera. The evolution of free surface is recorded by a fast video camera (Photron ULTIMA APX) as shown in Fig. 5. This device is supplied with a large, high sensitive CMOS sensor with a pixel array of 1024x1024 elements. The camera is able to acquire images at a time frequency up to 2000 frames per seconds with full resolution. Working frequency can be increased further by reducing the spatial resolution. Two other cameras with resolution 1024x1024 pixels and acquisition frequency 100 fps are used to record the global evolution of the flow field.

DAQ system. A data acquisition system (DAQ) is adopted for the acquisition of the wedge motion, through one potentiometer and two accelerometers, and the pressure evolution on the impact and top side of the wedge prism through six pressure transducers (see Fig. 6). The potentiometer and the accelerometers are not placed on the wedge prism but on the sliding beam (around the middle). A

trigger signal is generated when the magnet of the release mechanism is switched off. This signal, recorded by the DAQ system, ensures the synchronization between the DAQ system and the images of the high speed camera.

Four different Froude numbers are investigated by varying the freefall height. The test matrix is presented in Table 1. For each case, the test is repeated 10 times in order to ensure a good repeatability. For the high-speed camera, a frame rate of 1000 frames per second is used in order to capture the oscillation of the closed cavity. A sampling rate of 20 kHz is used for the DAQ system. The vertical velocity of the wedge cylinder is obtained in two ways: by differentiating the position with respect to time and by integrating the acceleration w.r.t. time.

2.2 A typical procedure for water entry of a freefall wedge

In order to characterize the kinematic and dynamic evolution of the water entry of a freefall wedge we refer to the test case 2. Fig. 7 shows the time histories of the acceleration (top panel), of the pressure evolution recorded both by the three sensors P4, P5 and P6 (middle panel) located on the impact side of the wedge and the three sensors P1, P2 and P3 (bottom panel) located on the roof of the wedge. Fig. 8, illustrating the images of the fast camera synchronized with the signals of the sensors, helps the comprehension of the phenomena involved. Four stages (see the top panel of Fig. 7) are identified: slamming (stage A), transition (stage B), collapse (stage C) and post-closure (stage D). At the beginning of the impact, stage A, the water rises up along the wedge and jet flows are formed at the body sides. An impulsive load occurs (see the middle panel of Fig. 7). In the present case, stage A is characterized by a nearly linear increase of the wedge acceleration (see the first panel of Fig. 7). Because of the short rise time which characterizes the impulsive local load, a hydroelastic reaction of the local structure may be triggered when the rising time is comparable to a typical natural period of the structural mode contributing to large structural stresses [11]. In the present case, the highest natural period associated with the first structural mode of the wedge is smaller than the rising time of the local load. When the jet reaches the knuckle of the wedge, non-viscous flow separation occurs. The jet then breaks up into spray. When the root of the jet/spray leaves the knuckle of the wedge (see the subplot a) of Fig. 8), the transition stage, i.e. the stage B, starts. The rate of change of the added mass reduces significantly causing the strong drop of the slamming force which corresponds to the strong drop of the wedge acceleration (see the top panel of Fig. 7, stage B). When the root of the spray is far away from the knuckle of the wedge (as shown in the subplot b) of Fig. 8), the transition stage ends and the collapse stage (stage C) starts. During the evolution of the stage C, the acceleration of the wedge (or the hydrodynamic loads) changes slowly (see the top panel of Fig. 7). The collapse stage ends just before the closure of the cavity, which is shown in the subplot c) of Fig. 8. After the closure of the cavity, the air compressibility matters inducing an oscillation of the cavity pressure (see the bottom panel of Fig. 7) and of the wedge acceleration (see the top panel of Fig. 7, stage D). As a consequence of the oscillation motion of the body, the pressure time history of the transducers P4, P5 and P6 (on the impact side) will oscillate at the same frequency of the wedge acceleration (see stage D of the middle panel of Fig. 7). Note that the amplitude of the pressure oscillation on the roof of the wedge during the stage D (see the bottom panel of Fig. 7) is comparable with the peak pressure recorded by the transducers P4, P5 and P6 during the slamming stage. The behavior confirms the dangerousness of the air-compressibility effects to the local structure. Further, when air-compressibility matters, the Euler number is important for a proper scaling of local loads [12-13].

3. Mathematical model

The above experimental observations are useful to guide the proper choice of the numerical or theoretical models for the investigation of the physical phenomena involved. In particular, during the water entry of a freefall wedge, a cavity can be created on the top of the wedge. Since the density of water is much larger than the density of air (and provided that the wedge velocity is much less than the speed of sound), the air flow can be safely neglected during most of the period before the closure of the cavity. Close to the pinch-off of the cavity, the gap width near the closure point that the air flows through goes to zero, and the velocity of the air will diverge under the assumption of the incompressibility of the air. Although in reality the compressibility of the air limits the air speed, it can even reach supersonic speeds [14]. It implies that the air flow plays an important role close to the moment of the pinch-off. In this section, first a single-fluid model is presented to reproduce the water entry of the freefall wedge without considering the air flow. Then an incompressible two-fluid model is developed to investigate the influence of the air flow in particular at the end of stage C. After the closure, the air compressibility matters. Another double-fluid model (incompressible water and compressible air) must be considered.

3.1 Single-fluid formulation

We assume that a two-dimensional wedge with mass M, deadrise angle β and beam $2c_0$ vertically impacts the still water surface with initial entry speed V_0. Since the density of water is much larger than the density of air and the wedge velocity is much less than the speed of sound, we may safely neglect the air flow. Let ρ_w be the density of water and μ the dynamic viscosity of water. Because of the short duration of impact, viscous effects can be neglected provided that the Reynolds number $\mathrm{Re} = \rho_w V_0 c_0/\mu \gg 1$. Further, we assume the water incompressible and the flow irrotational. Therefore a velocity potential satisfying Laplace's equation

$$\nabla^2\varphi = 0 \tag{1}$$

is introduced. The local water velocity is given by $\mathbf{u} = \nabla\varphi$. Using Green's second identity, the two-dimensional velocity potential can be represented in the boundary integral equation (BIE):

$$\theta\cdot\varphi(y,z) = \int_{\partial\Omega} [\log r\mathbf{n}\cdot\nabla\varphi - \varphi\mathbf{n}\cdot\nabla\log r]ds(\xi,\eta) \quad . \tag{2}$$

Here, (y,z) are the field point coordinates, (ξ,η) are the integration coordinates, $r = \sqrt{(\xi-y)^2+(\eta-z)^2}$, and $\mathbf{n}$ denotes the interior normal to the boundary $\partial\Omega$ of the water domain Ω. In the water, θ is equal to 2π. On $\partial\Omega$, θ is the local interior angle of the boundary.

The flow is symmetric about the central line, y=0, of the domain Ω. We can then simulate only half of the fluid domain Ω. Fig. 9 shows the coordinates and definitions of the computational domain.

On the wedge surface the impermeability boundary condition holds

$$\frac{\partial\varphi}{\partial n} = \mathbf{V}\cdot\mathbf{n} \,. \tag{3}$$

Similarly, the boundary conditions on the fixed bottom, at the control line S_C and at the truncation boundary far away from the body are

$$\frac{\partial\varphi}{\partial n} = 0 \,. \tag{4}$$

Eq. (4) is the exact boundary condition at the ends of the tank to reproduce the experiments. For open ocean (infinite domain), this represents an approximation at the truncation boundary. On the free

surface, fully nonlinear kinematic and dynamic boundary conditions are satisfied

$$\frac{Dy}{Dt}=\frac{\partial\varphi}{\partial y},\frac{Dz}{Dt}=\frac{\partial\varphi}{\partial z} \tag{5}$$

$$\frac{D\varphi}{Dt}=\frac{1}{2}|\nabla\varphi|^2-gz \tag{6}$$

Here the operator

$$\frac{D}{Dt}=\frac{\partial}{\partial t}+\frac{\partial\varphi}{\partial y}\frac{\partial}{\partial y}+\frac{\partial\varphi}{\partial z}\frac{\partial}{\partial z}$$

is the substantial derivative following the water particle on the free surface. In the dynamic boundary condition, the surface tension σ has been neglected by assuming the Weber number $W=\rho_w V_0^2 c_0/\sigma\gg 1$. Before the closure of the cavity, the pressure on the free surface is assumed to be the atmospheric pressure p_a.

The motion of the wedge is calculated by Newton's second law

$$M\dot{\mathrm{V}}=F_z-Mg \tag{7}$$

with

$$\frac{dZ_G}{dt}=\mathrm{V}\,. \tag{8}$$

Here F_z is the total vertical force due to the water pressure and Z_G the vertical position of the wedge center of mass.

The numerical hydrodynamic forces acting on the wedge are obtained by integrating p over the wetted wedge surface. From Bernoulli's equation, the pressure on the wedge surface can be evaluated by

$$p-p_a=-\rho_w(gz+\frac{\partial\varphi}{\partial t}+\frac{1}{2}|\nabla\varphi|^2)\,. \tag{9}$$

This requires evaluating the $\partial\varphi/\partial t$ term, which is unknown before we solve for it. The $\partial\varphi/\partial t$ term can be evaluated by solving the boundary value problem for the function $\psi=\partial\varphi/\partial t$, which is still governed by 2D Laplace equation.

3.2 Two-fluid formulation

We assume that a two-dimensional wedge with mass M, deadrise angle β, beam $2c_0$ vertically impacts the still water surface with initial entry speed V_0. Provided that the Reynolds number $\mathrm{Re_{w,a}}=V_0c_0/\nu_{\mathrm{w,a}}\gg 1$ and due to the short duration of impact, viscous effects can be neglected. Here, the subscript 'w' and 'a' indicate the water and the air respectively, and $\nu_{\mathrm{w,a}}$ are the kinematic viscosities of water and air. Further, we assume that both water and air are incompressible and the flow is irrotational. Then the velocity potentials φ_{w} and φ_{a} satisfying Laplace's equation

$$\nabla^2\varphi_{w,a}=0 \tag{10}$$

are introduced. The local velocity is given by $\mathbf{u}=\nabla\varphi$. Using Green's second identity, the two-dimensional velocity potentials can be represented as BIEs:

$$\theta_{w,a}\cdot\varphi_{w,a}(y,z)=\int_{\partial\Omega}[\log r\mathbf{n}\cdot\nabla\varphi_{w,a}-\varphi_{w,a}\mathbf{n}\cdot\nabla\log r]ds(\xi,\eta)\quad . \tag{11}$$

Here (y,z) are the field point coordinates, (ξ,η) are the integration coordinates, $r=\sqrt{(\xi-y)^2+(\eta-z)^2}$, and $\mathbf{n}$ denotes the interior normal to the boundary $\partial\Omega_{\mathrm{w,a}}$ of the domain $\Omega_{w,a}$ of a fluid. In the fluid, $\theta_{w,a}$ is 2π. On $\partial\Omega$, $\theta_{w,a}$ is the local interior angle of the boundary.

As for the single-fluid formulation, the flow is symmetric about the central line, y=0, of the domain Ω, which allows the solution of the problem to be found only in half of the fluid domain Ω. Fig. 10 shows the coordinates and definitions of the computational domain. Two truncation boundaries S_I and S_{II} are introduced to reduce the computational effort. They are far away from the wedge in order to assume the fluids are undisturbed along the truncation boundaries. On the wedge surface the boundary condition is given by

$$\frac{\partial \varphi_{w,a}}{\partial n} = \mathbf{V} \cdot \mathbf{n} \,. \tag{12}$$

It means that the fluid cannot penetrate the body. Similarly, the boundary condition on the fixed bottom is

$$\frac{\partial \varphi_{w}}{\partial n} = 0 \,. \tag{13}$$

At the control line S_C, the boundary condition is exactly

$$\frac{\partial \varphi_{w,a}}{\partial n} = 0 \,. \tag{14}$$

At the vertical truncation boundary S_I, the boundary condition is approximated by

$$\frac{\partial \varphi_{w,a}}{\partial n} = 0 \,. \tag{15}$$

At the horizontal truncation boundary S_{II}, the velocity potential of air and its time derivative are specified

$$\varphi_a = 0 \tag{16}$$

and

$$\frac{\partial \varphi_{a}}{\partial t} = 0 \,. \tag{17}$$

The boundary integral equations are coupled through the continuity condition of normal speed, i.e.

$$\frac{\partial \varphi_a}{\partial n_a} = -\frac{\partial \varphi_w}{\partial n_w} \,. \tag{18}$$

Moreover, we have the continuity condition of pressure on the air-water interface

$$\rho_a \left(\frac{\partial \varphi_a}{\partial t} + \left|\nabla \varphi_a\right|^2 / 2 + gz\right) = \rho_w \left(\frac{\partial \varphi_w}{\partial t} + \left|\nabla \varphi_w\right|^2 / 2 + gz\right) \,. \tag{19}$$

Here, the surface tension σ has been neglected by assuming the Weber number

$$W = \rho_w V_0^2 c_0 / \sigma \gg 1.$$

The boundary integral equations (11) with the boundary conditions (12)-(16) and (18)-(19) are solved to obtain the unknown velocity potential and the normal derivative of velocity potential. To track the evolution of air-water interface, the fully nonlinear kinematic and dynamic boundary conditions are applied

$$\frac{Dy}{Dt} = \frac{\partial \varphi_w}{\partial y} \,, \frac{Dz}{Dt} = \frac{\partial \varphi_w}{\partial z} \tag{20}$$

$$\frac{D(\rho_w \varphi_w - \rho_a \varphi_a)}{Dt} = \underline{\mathbf{V}} \cdot \nabla (\rho_w \varphi_w - \rho_a \varphi_a) + \rho_a \left(\left|\nabla \varphi_a\right|^2 / 2 + gz\right) - \rho_w \left(\left|\nabla \varphi_w\right|^2 / 2 + gz\right) \,. \tag{21}$$

Here, $\underline{\mathbf{V}} = \left(\frac{\partial \varphi_w}{\partial y}, \frac{\partial \varphi_w}{\partial z}\right)$ is the advection velocity of the water particle on the air-water interface and

$$\frac{D}{Dt} = \frac{\partial}{\partial t} + \underline{\mathbf{V}} \cdot \nabla$$

is the substantial derivative following the water particle on the air-water interface. After the occurring

of flow separation at the knuckle, the knuckle point becomes the contact point between the air-water interface and the wedge surface. To track the evolution of the velocity potential at the knuckle, the substantial derivative should follow the knuckle point and therefore $\underline{\mathbf{V}}$ should represent the velocity of the knuckle point, which is equal to the velocity of the wedge, i.e. (0, -V).

Newton's second law (see Eqs. (7)-(8)) is used to calculate the rigid body motion. The aero-hydrodynamic forces are achieved through the pressure integration along the body surface. Bernoulli's equation provides the pressure on the wedge surface

$$p = -\rho_{w,a}(gz + \frac{\partial \varphi_{w,a}}{\partial t} + \frac{1}{2}\left|\nabla \varphi_{w,a}\right|^2) \quad . \tag{22}$$

The $\partial \varphi_{w,a}/\partial t$ terms in Eq. (22) are unknown. They can be evaluated by solving the boundary value problem for the functions

$$\psi_{w,a} = \partial \varphi_{w,a} / \partial t \,, \tag{23}$$

which are also governed by the 2D Laplace equation

$$\frac{\partial^2 \psi_{w,a}}{\partial y^2} + \frac{\partial^2 \psi_{w,a}}{\partial z^2} = 0 \,. \tag{24}$$

Again these functions are transformed to the boundary integral equations:

$$\theta_{w,a} \cdot \psi_{w,a} = \int_{\partial\Omega} [\log r \mathbf{n} \cdot \nabla \psi_{w,a} - \psi_{w,a} \mathbf{n} \cdot \nabla \log r] ds \quad . \tag{25}$$

Along the symmetric line and the truncation boundary S_I, the boundary condition is exactly

$$\frac{\partial \psi_{w,a}}{\partial n} = 0 \,. \tag{26}$$

Similarly, the boundary condition on the bottom is

$$\frac{\partial \psi_w}{\partial n} = 0 \,. \tag{27}$$

On the truncation boundary S_{II}, we have

$$\psi_a = 0 \,, \tag{28}$$

which is consistent with Eq. (17). On the wetted body surface, we have the same boundary condition as for the single-fluid flow [9], i.e.

$$\frac{\partial \psi_w}{\partial n} = \dot{\mathbf{V}} \cdot \mathbf{n} + \frac{\partial \varphi_w}{\partial n} \frac{\partial^2 \varphi_w}{\partial s^2} \,. \tag{29}$$

Similarly, on the dry body surface, i.e. the top side of wedge, the boundary condition is

$$\frac{\partial \psi_a}{\partial n} = -\dot{\mathrm{V}} - \mathrm{V} \frac{\partial^2 \varphi_a}{\partial s^2} \,. \tag{30}$$

Eq. (19) gives one boundary condition on the air-water interface as

$$\rho_w \psi_w - \rho_a \psi_a = \rho_a(\left|\nabla \varphi_a\right|^2 / 2 + gz) - \rho_w(\left|\nabla \varphi_w\right|^2 / 2 + gz) \quad . \tag{31}$$

In addition on the air-water interface the continuity condition of normal speed, i.e. Eq. (18), should be always satisfied. This implies that, another boundary condition or constraint condition should be applied as the following

$$(\frac{\partial}{\partial t} + \frac{\partial \varphi_w}{\partial n_w} \frac{\partial}{\partial n_w})(\frac{\partial \varphi_a}{\partial n_a} + \frac{\partial \varphi_w}{\partial n_w}) = 0 \,,$$

which gives

$$\frac{\partial \psi_a}{\partial n_a} + \frac{\partial \psi_w}{\partial n_w} = \frac{\partial \varphi_w}{\partial n_w}(\frac{\partial^2 \varphi_w}{\partial s_w^2} - \frac{\partial^2 \varphi_a}{\partial s_a^2}) \,. \tag{32}$$

Solving Eq. (25) with the boundary conditions (26)-(32), the $\partial \varphi_{w,a}/\partial t$ terms can be obtained and then the pressure along the boundaries can be evaluated through the Bernoulli's equation, i.e. Eq. (22).

The two-fluid formulation represents the air and water flows by two sets of the boundary integral equations, which are coupled through the continuity conditions on the air-water interface. In the following section, we present the methodologies to solve the boundary integral equations (11) with the

boundary conditions (12)-(16) and (18)-(19) for the velocity potential and the BIEs (25) with the boundary conditions (26)-(32) for the $\partial\varphi/\partial t$ term, in order to follow the evolution of the air-water-wedge system.

4. Numerical method

The BIEs, e.g. Eq. (2) and Eq. (11), are solved using boundary element methods (BEM). The equations of the wedge motion are solved by the explicit Euler method and the air-water interface is tracked by following the water particles on it and using the second-order Runge-Kutta method. In the following, the numerical method for the single-fluid model is referred as 'single-fluid BEM' and the numerical method for the two-fluid model as 'two-fluid BEM'. The reader who is interested in the detailed description of the single-fluid BEM can refer to [9]. Here we discuss only the two-fluid BEM.

4.1 Numerical solutions of BIEs

To solve the BIEs (11), the linear BEM is utilized: the boundary of the water and air domain is represented by a set of straight line segments (elements); the functions φ_w, φ_a, $\partial\varphi_w/\partial n_w$ and $\partial\varphi_a/\partial n_a$ are assumed to vary linearly along each element; all unknown nodal values of φ_w, φ_a, $\partial\varphi_w/\partial n_w$ and $\partial\varphi_a/\partial n_a$ need to be solved; a linear equation system for the unknown nodal values of φ_w, φ_a, $\partial\varphi_w/\partial n_w$ and $\partial\varphi_a/\partial n_a$ is built by evaluating the BIEs (11) at each node; solve the linear equation system; once all nodal values of these functions are known, the velocity potential at any given field point can be approximated through BIEs (11). On the air-water interface, a node has four unknown nodal values, φ_w, φ_a, $\partial\varphi_w/\partial n_w$ and $\partial\varphi_a/\partial n_a$ and we need choose a proper equation for each unknown nodal value; on the remaining boundaries, a node has only one unknown nodal value, φ_w or $\partial\varphi_w/\partial n_w$ or φ_a or $\partial\varphi_a/\partial n_a$, and it is natural to use the discretized version of Eq. (11) for the unknown nodal value. On the air-water surface we can use the BIEs (11), the continuity equation of normal speed (18) and

$$\rho_w\varphi_w - \rho_a\varphi_a = \Phi \tag{33}$$

to set up equations for the four unknown nodal values (note that Φ in Eq. (33) is known and governed by (21)). To avoid being ill-conditioned, the equation system should be built to be 'diagonally dominant'. Since the density of water is much larger than that of air, Eq. (33) is only suitable for φ_w, not for φ_a. On the air-water interface, when the discretized version of

$$\theta_w \cdot \varphi_w = \int_{\partial\Omega_w} [\log r\mathbf{n}\cdot\nabla\varphi_w - \varphi_w\mathbf{n}\cdot\nabla\log r]ds$$

is chosen for $\partial\varphi_w/\partial n_w$, the 'diagonally dominant' criterion could be also violated. To show this, we can consider the boundary integral along the two adjacent elements LC and CR with an interior intersection angle of $\theta_w(>\pi/2)$ for field point C. Assuming |LC|=|CR|=*l*, the boundary integral

$$\int_{LC+CR} [\log r\mathbf{n}\cdot\nabla\varphi_w - \varphi_w\mathbf{n}\cdot\nabla\log r]ds$$

is expressed as

$$\frac{l}{2}(\ln l-\frac{1}{2})\left(\frac{\partial\varphi_w}{\partial n_w}\right)_L + l(\ln l-\frac{3}{2})\left(\frac{\partial\varphi_w}{\partial n_w}\right)_C + \frac{l}{2}(\ln l-\frac{1}{2})\left(\frac{\partial\varphi_w}{\partial n_w}\right)_R .$$

By choosing a value of *l*=0.01, the coefficient of $(\partial\varphi_w/\partial n_w)_C$ is about -0.061, which is much less than θ_w, the dominant coefficient of $(\varphi_w)_C$. This drawback can be overcome by superimposing the boundary integral equations of water and air for the nodes on the air-water surface S_F:

$$\theta_w(P)\cdot\varphi_w(P)+\theta_a(P)\cdot\varphi_a(P)=\int_{\partial\Omega_w/S_F}[\log r\frac{\partial\varphi_w}{\partial n_w}-\varphi_w\frac{\partial\log r}{\partial n_w}]ds$$
$$+\int_{\partial\Omega_a/S_F}[\log r\frac{\partial\varphi_a}{\partial n_a}-\varphi_a\frac{\partial\log r}{\partial n_a}]ds \qquad \text{for } P\in S_F. \qquad (34)$$
$$+\int_{S_F}[\log r(\frac{\partial\varphi_a}{\partial n_a}+\frac{\partial\varphi_w}{\partial n_w})-\varphi_a(\frac{\partial\log r}{\partial n_a}+\frac{\partial\log r}{\partial n_w})]ds$$

Here, the term

$$\frac{\partial\varphi_a}{\partial n_a}+\frac{\partial\varphi_w}{\partial n_w}$$

is known and equal to zero. Then, we can build a closed linear equation system free of the unknown nodal value $\partial\varphi/\partial n$ on the air-water interface: Eq. (33) is used for the unknown nodal value φ_w and Eq. (34) for φ_a on the air-water interface; Eq. (11) is used for the unknown nodal values on other boundaries. After this linear equation system is solved, all nodal values except for $\partial\varphi/\partial n$ on the air-water interface become known. In order to obtain $\partial\varphi/\partial n$ on the air-water interface, we solve the single-fluid boundary integral equation for the problem in water by using Dirichlet boundary condition (prescribing φ_w) on the air-water interface.

The $\partial\varphi/\partial t$ term can be solved in a similar way. We note that the term

$$\frac{\partial\psi_a}{\partial n_a}+\frac{\partial\psi_w}{\partial n_w}$$

is non-zero but known and it contributes to the right hand side terms of the linear equation system.

4.2 Time-marching procedure.

The wedge motion and the evolution of air-water interface are governed by Eqs. (7), (8), (20) and (21). At the time step *n*, the configuration of the air-water interface, the potential difference Φ on the air-water interface, the position Z_G and the velocity V of the wedge are known. A proper time integration scheme should be applied to Eqs. (7), (8), (20) and (21) to get these variables at the new time step *n*+1. Further, the motion of the wedge is coupled with the air-water flow: the calculation of the acceleration $\dot{V}$ requires evaluating the vertical hydrodynamic force F_z, which is unknown before solving the BIEs for the velocity potential and the $\partial\varphi/\partial t$ term; the velocity V and/or the acceleration $\dot{V}$ of wedge are used to construct the body boundary conditions for the solution of the velocity potential and the $\partial\varphi/\partial t$ term. In the present method, the motion of wedge and the fluid flow are solved in a decoupled manner. The motion of the wedge is solved by the explicit Euler method, while the evolution of the air-water interface is solved by the second order Runge-Kutta method. The detailed time-marching procedure is described in Appendix A.

5. Results

5.1 Comparison of experiments and numerical results

During the water entry of the wedge, the air velocity should be of the same order of the water velocity near the air-water interface and the wedge velocity near the wedge body, both of which are small compared to the speed of sound for the present cases. Far away from the wedge, the air velocity is negligible. Close to the pinch-off of the cavity formed on the top of the wedge, the water tends to 'compress' the air cavity, causing the increase of the pressure inside the cavity and the air flow out of the cavity. Only when the gap (where the air flows out of the cavity) becomes narrow, the escape velocity of the air becomes large (comparable to the speed of sound). Therefore, during most of the period before pinch-off, the air flow can be safely neglected (since the density of the water is much

larger than that of the air) and the single-fluid model is suitable for simulating the water entry of the freefall wedge. In this section, the results of the single-fluid numerical model are compared to the experiments to verify/validate the numerical method and integrate the experimental data for a proper physical understanding of the phenomena involved. The emphasis is on the pressure distribution on the impact side (through the time histories of the pressure tranducers P4, P5, and P6 as shown in Figs. 14-17), on the wedge motion (Figs. 11-13), and on the evolution of free surface (Figs. 18-21). Note that the numerical pressure is computed at the center of the sensitive surface of the pressure transducer. All experimental results are the average values based on 10 repeated tests with the corresponding standard deviations (error bars). Because the standard deviation of the draft is as small as $O(10^{-3})$ and therefore not shown in the plots.

In general the results of the numerical method agree well with the experimental results except that there are clear differences in measured and numerically predicted peak body acceleration for cases 2-4. When we have peak acceleration, the numerical pressures on the impact side agree well with experiments, which should result in a good agreement of the hydrodynamic force (and the body acceleration) between the numerical results and experiments. This causes a contradiction that we cannot explain. The fact that both the numerical pressures and global free surface elevation agree well with experiments makes us believe that the single-fluid BEM can accurately simulate the water entry of the freefall wedge before the closure of the cavity.

5.2 Comparison of single-fluid BEM and two-fluid BEM

In this subsection, the proposed two-fluid BEM is used to investigate the influences of the air flow before the closure of the cavity (stage C) and to investigate the air flow inside the cavity. During the evolution of stage C, the results of the two-fluid BEM are compared with the ones of the single-fluid BEM. The cross-section data of wedge used in the present numerical analysis are the same as those used in the experiments and the initial water-entry speed of the wedge is 0.93 m/s (which corresponds to the experimental case 2). Up to the closure of the cavity, the impact lasts about 0.33 s. In order to avoid the simulation of the jet flow and to reduce the computational effort, the two-fluid BEM solver starts at about t=0.05 s, i.e. close to the end of stage B. This is a conservative choice since at this time instant the influence of the air flow is still negligible. Because of the assumed incompressibility of the air, the gap width near the pinch-off point through which the air flows out goes to zero, causing the velocity of the air to diverge. To avoid the singularity, the numerical simulation by the two-fluid BEM is stopped when the gap between the air-water interface and the vertical symmetrical boundary is less than a prescribed tolerance ε. In the present simulation, ε is set to be 1.5 mm, that is the numerical simulation stops at t=0.33017s. First, the conservation of fluid mass and energy is checked and the details are presented in Appendix B. It can be seen that the conservation of mass and energy of the air, water and air-water system is well satisfied. Fig. 22 compares the draft, velocity and acceleration of the wedge, respectively. In general, the results obtained by the two-fluid BEM agree well with the results of the single-fluid BEM. However, close to the pinch-off of the cavity, the water motion tends to compress the air cavity on the top of the wedge, inducing an increase of the air pressure inside the cavity. This justifies a significant increment of the wedge acceleration (about 1 m/s^2) and a slight increment of the wedge speed (about 0.03 m/s) in the downwards direction, compared to the results by the single-fluid BEM (see the subplot c) and b) of Fig. 22 respectively). Note that the behavior predicted by the two-fluid model is consistent with the experimental observation (see the first panel of Fig. 7 at the end of stage C, or the subplot b) of Fig. 13).

Fig. 23 compares the free surfaces predicted by the single-fluid BEM and two-fluid BEM at several

time instants from the start of the two-fluid BEM to the pinch-off of the cavity, and almost perfect agreements are obtained. The fine differences are examined by comparing the free surfaces close to the pinch-off of the cavity: Fig. 24 shows the results around the cavity and Fig. 25 shows the results around the pinch-off point. The following results are observed: even close to the pinch-off of the cavity, the free surface predicted by the two-fluid BEM agrees very well with that by the single-fluid BEM except near the pinch-off point; near the pinch-off point, the evolution of the free surface by the two-fluid BEM is slightly slower than that by the single-fluid BEM (lag of 1 mm), which is probably due to the cumulative effect of the air resistance. We note that, very close to the pinch-off of the cavity, the air flow speed near the pinch-off point becomes very large and therefore very large negative pressure is induced. The large negative pressure results in the suction force on the free surface, which can accelerate the pinch-off of the cavity.

To investigate the cumulative effect of the air flow further, the velocity potential of the water and the normal velocity on the free surface around the cavity are compared at time t=0.33017 (which is just before closure), and the results are presented in Figs. 26-27. It is found that, except for a small region near the pinch-off point, the results of the single-fluid BEM agree well with the results of two-fluid BEM. It seems that the cumulative effect of the air flow is very limited and the air flow can be safely neglected during most of the period before the pinch-off of the cavity.

Figs. 28-29 show the vertical velocity component of air and the pressure along the cavity wall and the symmetric boundary at time t=0.33017 (slightly before the closure). Fig 30 shows the pressure inside the cavity at time t=0.33017. It is observed that the vertical velocity of the flow inside the cavity is of the same order of the vertical velocity of wedge, and the pressure inside the cavity is quite uniform and significantly increased. Near the pinch-off point, because of the small escape area the air flow speed is very large inducing large negative pressure.

In general, a satisfactory agreement between the incompressible two-fluid BEM and the single-fluid BEM is obtained. However, close to the pinch-off of the cavity on the top of the wedge, the water tends to 'compress' the air cavity and the pressure of the air cavity increases significantly, which results in a significant increment of the wedge acceleration and a slight increment of the wedge speed in the downwards direction, compared to the results by single-fluid BEM. The increment of the pressure inside the cavity acts as resistance and results in the contraction of the cavity being slightly slower than that predicted by the single-fluid BEM. The numerical results show that this influence is limited: only close to the pinch-off and near the pinch-off point, the free surface and the contraction speed (normal speed) is slightly different from those predicted by the single-fluid BEM. This indicates that the air flow matters just before the pinch-off of the cavity, which is different from the closure mechanism of three-dimensional cavity. Peters *et al.* [15] studied the air flow in a collapsing cavity created by the impact of a circular disc on a water surface and reported that the air flow starts to play an important role at R/R_0=0.2, where R is the radius of the cavity neck (this corresponds to the minimum gap area) and R_0 is the radius of the disk. The reason for this is that the parameter, which characterizes the importance of the air flow, is the area of the gap. For a 3D cavity, the area of the gap is represented by $(R/R_0)^2$, but it is R/R_0 for 2D cavity. Based on the study by Peters *et al.*, we estimate that for the present case the air flow starts to play an important role when the gap reduces to about

$$c_0\,(0.2)^2 \approx 3 \text{ mm}.$$

This agrees with our numerical results. Therefore, it can be concluded that, for the closure of 2D cavity, the air flow starts to play an important role just before the closure and due to the short duration the influence of air flow on the body velocity and configuration of the air-water interface is limited.

In reality, the air is compressible. Because the single-fluid BEM assumes no influence from the air flow, it should be equivalent to a two-fluid solver which assumes that the compressibility of air is infinite. Therefore, the results of the single-fluid BEM and the results of the incompressible two-fluid BEM can be regarded to be an 'upper bound' and an 'lower bound' (or an 'lower bound' and an 'upper bound') of the results of real flow respectively. Since the results of the single-fluid BEM agree well with those of the incompressible two-fluid BEM, the conclusions/results from the incompressible two-fluid BEM can also apply to the real flow except that the real pressure inside the cavity could be a bit lower than that predicted by the incompressible two-fluid BEM. We conclude that just before the pinch-off the pressure inside the cavity becomes highly uniform and the flow of the air can be neglected.

The evolution of the cavity after closure can be represented in term of its pressure, which is characterized by the first peak pressure, decay rate and oscillation frequency, as in the similar of Abrahamsen & Faltinsen [16-17] who also consider the importance of heat exchange. For the present experiments, the aluminium wedge prism has thermal diffusivity much larger than that of water, so the heat exchange between the wedge and the cavity could dominate the heat exchange between the water and the cavity. The cavities on both sides of the longitudinal vertical wall are connected by the gap between the end of the wedge cylinder and the tank wall. They can interact with each other and cause air flow in the longitudinal direction. In fact, due to the existence of the guide tube, an air leakage could be formed during the oscillation of cavity, which causes a significant decay of the cavity pressure and leads to air flow in the longitudinal direction. All these effects should be taken into account when a mathematical model is specified for the post-closure stage.

6. Conclusion

Experiments were conducted to investigate the water entry of a freefall wedge. Experiments showed that a typical water entry of a freefall wedge can be divided into slamming, transition, collapse, and post-closure stages. At the beginning stage of impact, the water rises up and jets are formed at the body sides. During the impact, i.e. the slamming stage, impulsive loads occur. When the jet reaches the knuckle of the wedge, non-viscous flow separation occurs. The jet breaks up into spray. When the root of the spray leaves the knuckle of the wedge, the transition stage starts. During this stage, the rate of change of the added mass reduces significantly which leads to a strong drop of the slamming force and a corresponding drop in the acceleration. When the root of the spray is far away from the knuckle of the wedge, the transition stage ends and the collapses stage starts. During the collapse stage, the acceleration of wedge and the hydrodynamic loads change only slowly. The collapse stage ends just before the closure of the cavity, after which compressibility of air matters causing an oscillation of cavity pressure and wedge acceleration.

A single-fluid BEM is used to model the first three stages where results are compared to experiments to verify both the numerical method and the experiments. In general the results of the single-fluid BEM agree well with the experimental results except that the peak acceleration of the wedge is lower than that of the numerical results. We concluded that the experimental results are reliable expect for the peak pressure and the single-fluid BEM can accurately simulate the water entry of the freefall wedge before the closure of the cavity.

A two-fluid BEM was proposed to investigate the influence of the air flow during the collapse stage. It was concluded that just before the closure of 2D cavity, the air flow starts to play an important role in the cavity pressure, but due to the short duration the influence of air flow on the body velocity and

configuration of the air-water interface is limited. Further, the simulations by the two-fluid BEM highlight that just before the pinch-off, the pressure inside the majority of the cavity increases and tends to become uniform (so that the flow of the air inside the cavity can be neglected) but that near the pinch-off point, the air flow velocity is very large and negative pressure occurs here. After the closure of the cavity, the compressibility of the air plays an important role and leads to an oscillation of the cavity profile and pressure and the wedge acceleration.

Acknowledgement

This research activity has been partially supported by the Research Council of Norway through Centre for Ships and Ocean Structures (CeSOS), and is presently ongoing within the Centres of Excellence funding scheme AMOS, Project No. 223254. Part of the experiments at INSEAN has been also supported by the Flagship Project RITMARE – The Italian Research for the Sea – coordinated by the Italian National Research Council and funded by the Italian Ministry of Education, University and Research within the National Research Program 2011-2013. We thank the reviewers for their valuable comments and suggestions.

References

[1] Von Kármán T. The impact of seaplane floats during landing. NACA Tech. Note 321, Washington DC, 1929.

[2] Wagner H. Über Stoss- und Gleitvogänge an der Oberfläche von Flüssigkeiten. Z. Angew. Math. Mech. 1932;12: 193-235.

[3] Dobrovol' skaya ZN. On some problems of similarity flow of fluid with a free surface. J. Fluid Mech. 1969;36: 805-29.

[4] Cointe R, Armand JL. Hydrodynamic impact analysis of a cylinder. J. Offshore Mech. Arct. 1987; 109: 237-43.

[5] Greenhow M. Wedge entry into initially calm water. Appl.Ocean Res. 1987; 9(4): 214-23.

[6] Zhao R, Faltinsen OM . Water entry of two-dimensional bodies. J. Fluid Mech. 1993; 246: 593-612.

[7] Faltinsen OM. Water entry of a wedge with finite deadrise angle. J. Ship Res. 2002; 46: 39–51.

[8] Korobkin AA , Iafrati A . Hydrodynamic loads at the early stage of a floating wedge impact. In: Proc.17th Intern. Workshop on Water Waves and Floating Bodies, Cambridge, UK, 2002.

[9] Wang J, Faltinsen OM. Numerical Investigation for Air Cavity Formation During the High Speed Water Entry of Wedges. J. Offshore Mech. Arct. 2013; 135: n1.

[10] Wang J, Lugni C, Faltinsen, OM. Analysis of loads, motions and cavity dynamics during freefall wedges vertically entering the water surface. Submitted to this journal, 2014.

[11] Lugni C, Bardazzi A, Faltinsen OM and Graziani G. Hydroelastic slamming response in the evolution of a flip-through event during shallow-liquid sloshing. Phys. Fluids 2014;26: 032108.

[12] Lugni C, Miozzi M, Brocchini M, Faltinsen OM. Evolution of the air cavity during a depressurized wave impact. I. The kinematic flow field. Phys. Fluids 2010; 22: 056101.

[13] Lugni C, Brocchini M and Faltinsen OM. Evolution of the air cavity during a depressurized wave impact. II. The dynamic field. Phys. Fluids 2010; 22: 056102.

[14] Gekle S, Peters IR, Gordillo JM, van der Meer D, Lohse D. Supersonic air flow due to solid-liquid impact. Phys. Rev. Lett. 2010; 104: 024501.

[15] Peters IR, Gekle S, and Lohse D. Air Flow in a collapsing cavity. Phys. Fluids 2013; 25: 032104.

[16] Abrahamsen BC, Faltinsen OM. The effect of air leakage and heat exchange on the decay of entrapped air

pocket slamming oscillations. Phys. Fluids 2011; 23: 102107.

[17] Abrahamsen BC, Faltinsen OM. The natural frequency of the pressure oscillations inside a water-wave entrapped air pocket on a rigid wall. J. Fluid Struct. 2012; 35: 200-12.

Appendix A Time-marching procedure for the two-fluid BEM.

This section describes the time-marching procedure of solving Eqs. (7), (8), (20) and (21), which govern the wedge motion and the evolution of air-water interface. As described in section 4.2, the motion of the wedge is coupled with the air-water flow. In the present method, the motion of wedge and the fluid flow are solved in a decoupled manner, the motion of the wedge is solved by the explicit Euler method, and the evolution of the air-water interface is solved by the second order Runge-Kutta method. The detailed time-marching procedure is as follows:

1) Mesh the boundaries of air domain and specify the boundary conditions of air domain.
2) Build up the linear equation system for air-water flow by assembling BIEs in the way discussed in the section 4.1, and solve the linear equation system to obtain the φ on the air-water interface and the unknown variable, i.e. φ or $\partial\varphi/\partial n$ on other boundaries.
3) Use the φ on the air-water interface obtained in step 2) to construct the boundary conditions of the water flow, and build up and solve the linear equation system for the water flow to obtain $\partial\varphi_w/\partial n_w$; $\partial\varphi_a/\partial n_a$ on the air-water interface is obtained through Eq. (18).
4) Once φ is known, evaluate the tangential velocity $\partial\varphi/\partial s$ along all boundaries.
5) Construct the boundary conditions for the BIEs of the $\partial\varphi/\partial t$ term according to Eqs. (26)-(31), build up and solve the linear equation system for the $\partial\varphi/\partial t$ term. Note that we assume φ vary quadratically along the boundary among three adjacent nodes to calculate $\partial^2\varphi/\partial s^2$ in Eqs. (29)-(30).
6) Evaluate the pressure by Bernoulli's equation, i.e. (22) and integrate *p* over the wedge surface to obtain the vertical hydrodynamic force

$$F_z = -\int p n_z ds .$$

7) Determine the time step size by

$$\Delta t = \min\left\{\Delta t_1, C\min(\Delta h_i / u_i)\right\} .$$

Here Δt_1 is a prescribed time step size, *C* is a positive constant and chosen as 1 in the present calculations, *i* indicates a generic node on the air-water interface, Δh_i is the minimum distance from node *i* to the neighboring nodes and u_i is the velocity of node *i*.

8) Update the position of the wedge,

$$\frac{(Z_G)_{n+1} - (Z_G)_n}{\Delta t} = V_n . \tag{A.1}$$

9) Advect the air-water interface into the intermediate new position,

$$\frac{y^*_{n+1} - y_n}{\Delta t} = \left(\frac{\partial\varphi}{\partial y}\right)_n \tag{A.2}$$

$$\frac{z^*_{n+1} - z_n}{\Delta t} = \left(\frac{\partial\varphi}{\partial z}\right)_n \tag{A.3}$$

, and change the velocity potential difference on the air-water interface

$$\frac{\Phi_{n+1}^{*}-\Phi_{n}}{\Delta t}=\left(\underline{\mathbf{V}}\cdot\nabla(\rho_w\varphi_w-\rho_a\varphi_a)+\rho_a(|\nabla\varphi_a|^2/2+gz)-\rho_w(|\nabla\varphi_w|^2/2+gz)\right)_n . \quad (A.4)$$

Here, $\underline{\mathbf{V}}=(\frac{\partial\varphi_w}{\partial y},\frac{\partial\varphi_w}{\partial z})$ is the advection velocity of the water particle on the air-water interface, and the symbol '*' represents the intermediate time instant; at the knuckle, $\underline{\mathbf{V}}$ represents the velocity of the knuckle and is (0, -V).

10) Construct and mesh the intermediate boundaries of the water domain except the air-water interface.

11) The acceleration can be calculated using Eq. (7). However, if the vertical added mass A_{33} is much larger than M, numerical instability can occur. To improve numerical stability, Eq. (7) is re-written as

$$(M+A_{33})\dot{V}=F_z+A_{33}\dot{V}-Mg .$$

An accurate computation of A_{33} is difficult. However, it is unnecessary to compute A_{33} accurately. The above equation is equivalent to Eq. (7) even if A_{33} is an approximation. As long as A_{33} is a reasonable approximation, this method works without loss of accuracy. In the present simulation, A_{33} is approximated by

$$A_{33}=\frac{1}{2}\rho_w\pi c^2 ,$$

where c is the instantaneous half-wetted length measured on the calm water surface and is limited to the half breadth of the wedge. After A_{33} is estimated, an iterative scheme is constructed to compute the acceleration. As a first approximation, the acceleration of the wedge at time step n can be calculated as

$$(M+A_{33})\dot{V}_n=F_z+A_{33}\dot{V}_{n-1}-Mg . \quad (A.5)$$

12) Update the velocity of the wedge

$$\frac{V_{n+1}^{*}-V_n}{\Delta t}=\dot{V}_n \quad (A.6)$$

and

$$\frac{V_{n+1}-V_n}{\Delta t}=\dot{V}_n . \quad (A.7)$$

13) Update the body boundary condition at the intermediate stage by the intermediate body velocity.

14) At the intermediate stage, mesh the boundaries of the air domain and specify the associated boundary conditions.

15) At the intermediate stage, build up the linear equation system for air-water flow by assembling BIEs in the way discussed in section 4.1, and solve the linear equation system to obtain the φ_{n+1}^{*} on the air-water interface and the unknown variable, i.e. φ_{n+1}^{*} or $(\partial\varphi/\partial n)_{n+1}^{*}$ on other boundaries.

16) At the intermediate stage, use the φ_{n+1}^{*} on the air-water interface obtained by step 15) to construct the boundary conditions of the water flow, and build up and solve the linear equation system for the water flow to obtain $(\partial\varphi_w/\partial n_w)_{n+1}^{*}$; the $(\partial\varphi_a/\partial n_a)_{n+1}^{*}$ on the air-water interface is obtained by Eq. (18).

17) Based on φ^*_{n+1}, evaluate the tangential velocity $(\partial\varphi/\partial s)^*_{n+1}$ along all boundaries at the intermediate stage.

18) Time stepping the air-water interface by the second order Runge-Kutta method as

$$\frac{y_{n+1}-y_n}{\Delta t}=\frac{1}{2}\left(\frac{\partial\varphi}{\partial y}\right)_n+\frac{1}{2}\left(\frac{\partial\varphi}{\partial y}\right)^*_{n+1}, \tag{A.8}$$

$$\frac{z_{n+1}-z_n}{\Delta t}=\frac{1}{2}\left(\frac{\partial\varphi}{\partial z}\right)_n+\frac{1}{2}\left(\frac{\partial\varphi}{\partial z}\right)^*_{n+1}, \tag{A.9}$$

and

$$\begin{aligned}\frac{\Phi_{n+1}-\Phi_n}{\Delta t}=&\frac{1}{2}\left(\underline{\mathbf{V}}\cdot\nabla(\rho_w\varphi_w-\rho_a\varphi_a)+\rho_a(|\nabla\varphi_a|^2/2+gz)-\rho_w(|\nabla\varphi_w|^2/2+gz)\right)_n\\&+\frac{1}{2}\left(\underline{\mathbf{V}}\cdot\nabla(\rho_w\varphi_w-\rho_a\varphi_a)+\rho_a(|\nabla\varphi_a|^2/2+gz)-\rho_w(|\nabla\varphi_w|^2/2+gz)\right)^*_{n+1}\end{aligned}. \tag{A.10}$$

19) Perform cutting jet and/or spay by the method presented in [9].

20) Re-grid the air-water interface by the method presented in [9]. We note that the velocity potential difference Φ instead of the velocity potential φ is to be re-generated.

Appendix B Conservation of fluid mass and energy

This section checks the conservation of fluid mass and energy for the two-fluid BEM. Because fluid is assumed incompressible, the conservation of the fluid mass is equivalent to a zero change rate of the total volume of the fluid

$$\frac{d}{dt}\int_{\Omega_{w,a}}d\Omega=\int_{\partial\Omega_{w,a}}\frac{\partial\varphi_{w,a}}{\partial n}ds=0$$

, which results in the following ratio of one

$$R^{(M)}_{w,a}=-\int_{S_S}\frac{\partial\varphi_{w,a}}{\partial n}ds\Big/\int_{S_F}\frac{\partial\varphi_{w,a}}{\partial n}ds=1. \tag{B.1}$$

Here, S_S denotes the body boundary and S_F the air-water interface. Eq. (B.1) implies that the expansion of the air-water interface is equal to the volume displaced by the wedge. The energy of the fluid consists of the kinematical energy

$$E^{(\mathrm{K})}_{w,a}=\rho_{w,a}\int_{\Omega_{w,a}}\frac{1}{2}|\nabla\varphi_{w,a}|^2\,d\Omega$$

and the potential energy due to gravity

$$E^{(\mathrm{P})}_{w,a}=\rho_{w,a}\int_{\Omega_{w,a}}gz\,d\Omega.$$

The conservation of the fluid energy implies that the change rate of the total energy is equal to the work rate done by all external forces (excluding gravity force)

$$\frac{d}{dt}E_{w,a}=\frac{d}{dt}E^{(\mathrm{K})}_{w,a}+\frac{d}{dt}E^{(\mathrm{P})}_{w,a}=\frac{d}{dt}W_{w,a}.$$

For the present case, the external force is the force acting on the boundary of the fluid. Therefore, we have

$$\frac{d}{dt}W_{w,a} = \int_{\partial\Omega_{w,a}} p\frac{\partial\varphi_{w,a}}{\partial n}ds\,. \tag{B.2}$$

Further, it can be shown that

$$\begin{aligned}\frac{dE_{w,a}}{dt} = &-\frac{\rho_{w,a}}{2}\int_{\partial\Omega}\left(\psi_{w,a}\frac{\partial\varphi_{w,a}}{\partial n}+\varphi_{w,a}\frac{\partial\psi_{w,a}}{\partial n}\right)ds-\frac{\rho_{w,a}}{2}\int_{\partial\Omega}[\nabla\varphi_{w,a}\cdot\nabla\varphi_{w,a}]\frac{\partial\varphi_{w,a}}{\partial n}ds\\ &-\rho_{w,a}\int_{\partial\Omega}gz\frac{\partial\varphi_{w,a}}{\partial n}ds\end{aligned}\,. \tag{B.3}$$

Note that the air-water interface and body boundary have contribution to the integrals in Eqs. (B.2) and (B.3). The energy conservation of the air-water system is expressed as

$$\frac{d}{dt}E = \frac{d}{dt}E_w + \frac{d}{dt}E_a = \frac{d}{dt}W\,.$$

Here,

$$\frac{d}{dt}W = \int_{S_S} p\frac{\partial\varphi_{w,a}}{\partial n}ds\,. \tag{B.4}$$

The conservation of fluid energy is assessed through checking the ratios,

$$R_{w,a}^{(\mathrm{E})} = \frac{d}{dt}E_{w,a} / \frac{d}{dt}W_{w,a} \tag{B.5}$$

and

$$R^{(\mathrm{E})} = \frac{d}{dt}E / \frac{d}{dt}W \tag{B.6}$$

, which should be equal to one. Fig. B.1 checks the conservation of fluid mass and energy for case 2. It is observed that all ratios are around one and therefore the conservation of fluid mass and energy is well satisfied.

Figures

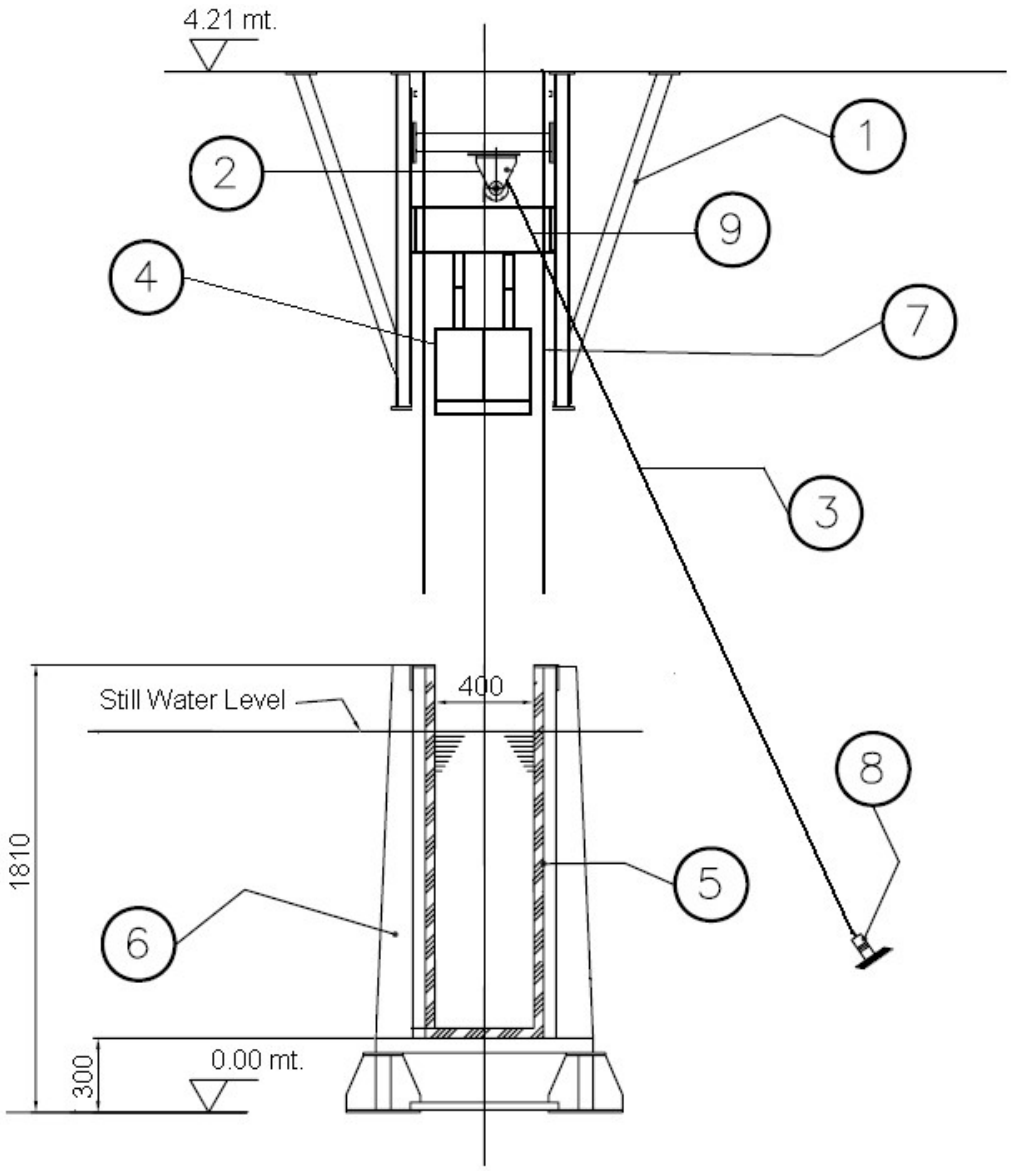

Fig. 1. Lateral view of the experimental apparatus. 1-support beam, 2-pulley, 3-cable, 4-cylinder, 5-tank, 6-structure of support, 7-linear guide, 8-electric magnet, 9-sliding beam.

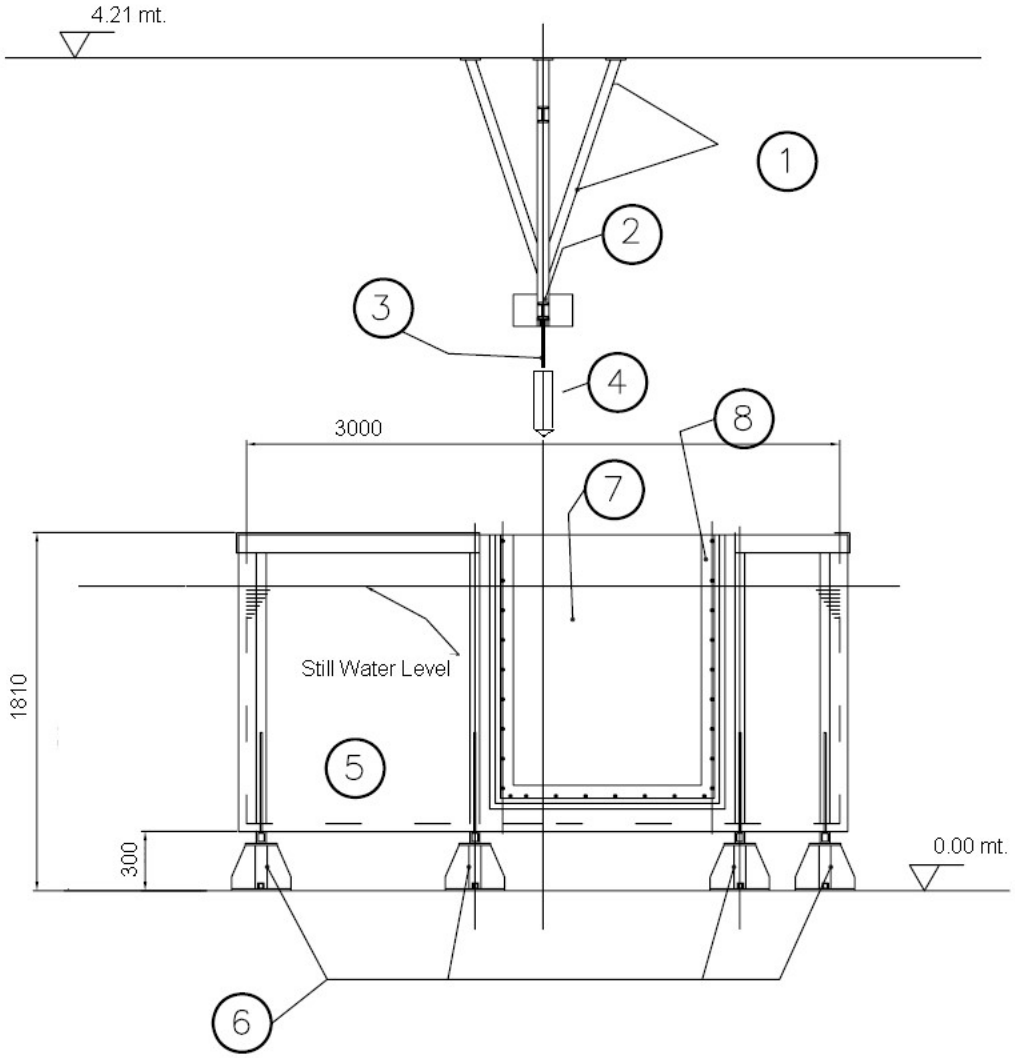

Fig. 2. Front view of the experimental apparatus. 1-support beam, 2-sliding beam, 3-linear guide, 4-cylinder, 5-tank, 6-structure of support, 7-Plexiglas window, 8-frame of the Plexiglas window.

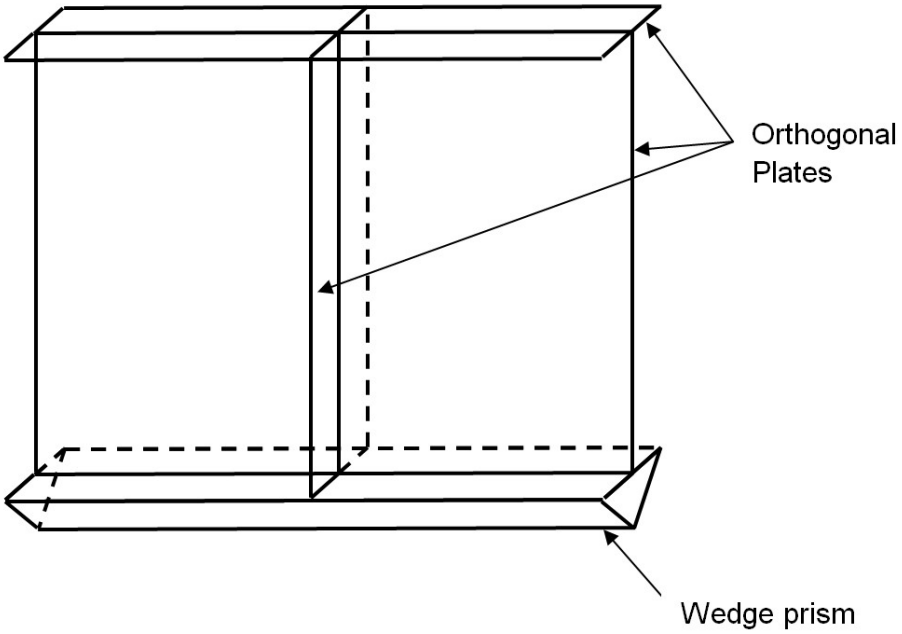

Fig. 3. Sketch of wedge cylinder

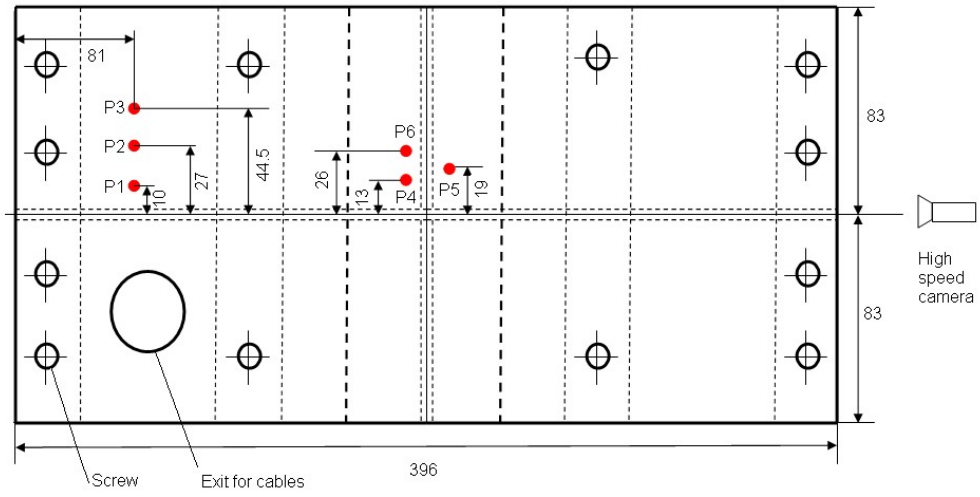

Fig. 4. Wedge prism arrangement (top view). Pressure transducer P1, P2 and P3 are on the top side of the wedge prism; P4, P5 and P6 are on the impact side.

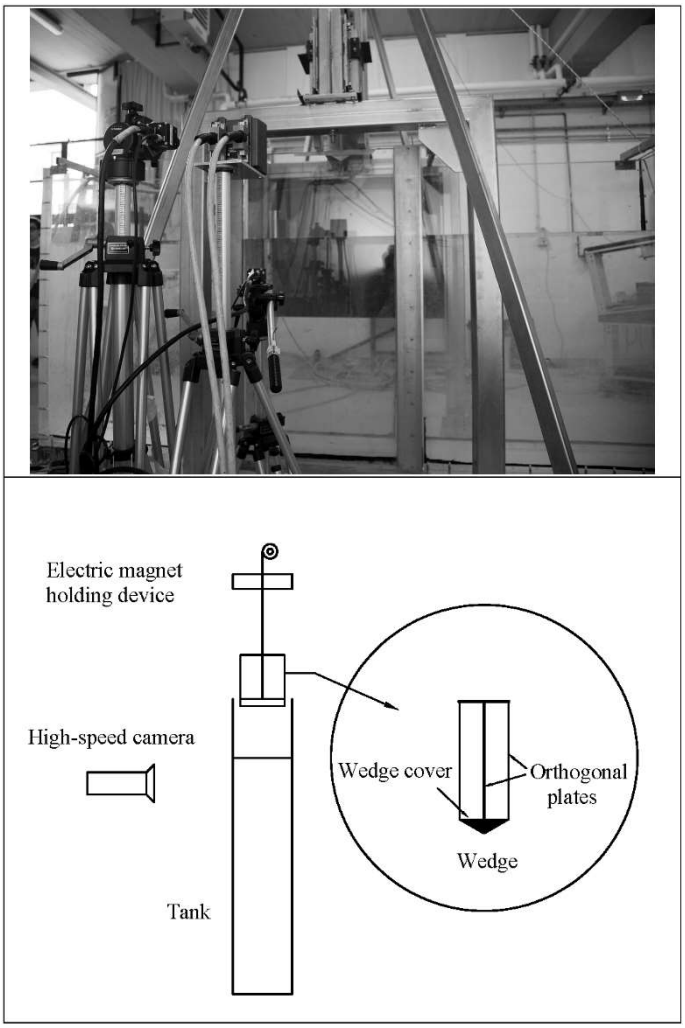

Fig. 5. Camera set-up.

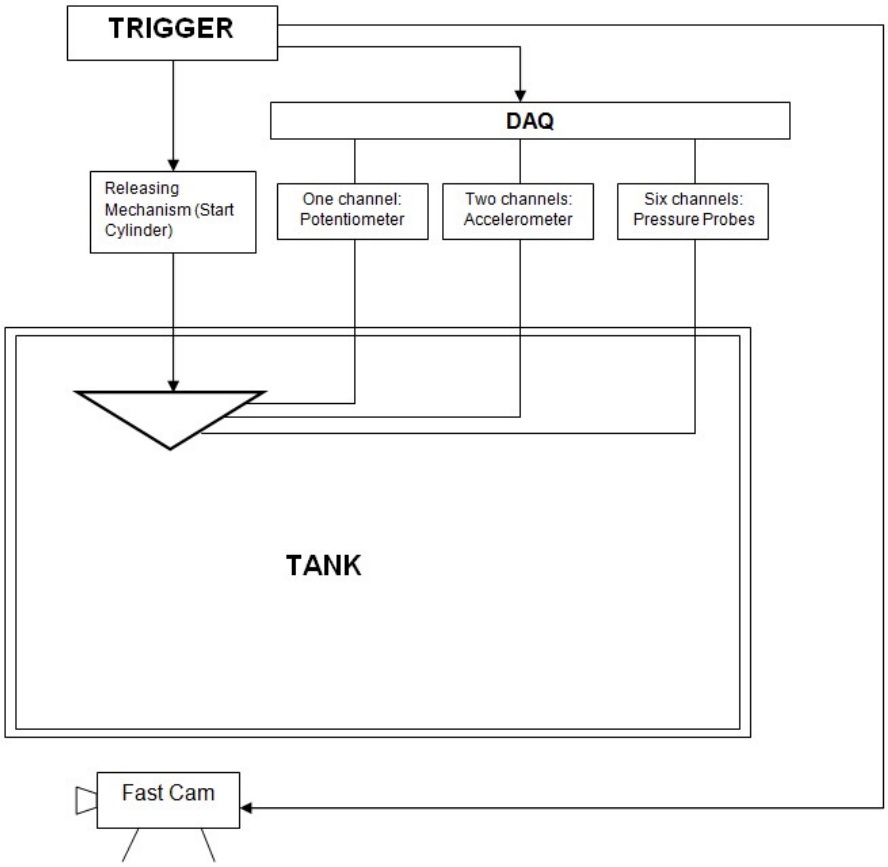

Fig. 6. Global sketch of the experimental set-up.

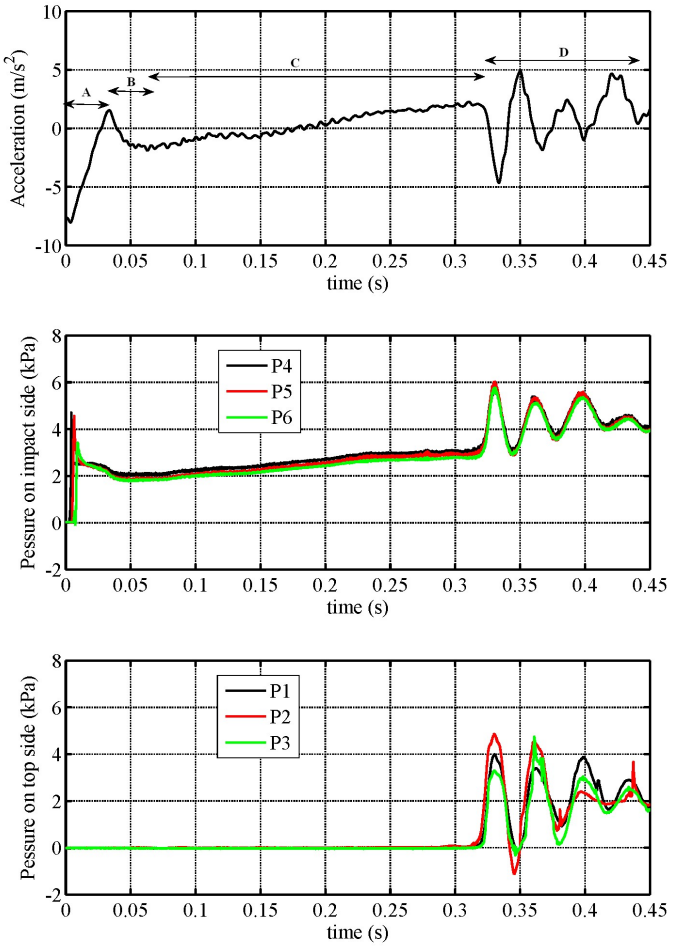

Fig. 7. An experimental measurement of the wedge acceleration and pressures the on wedge body for test case 2.

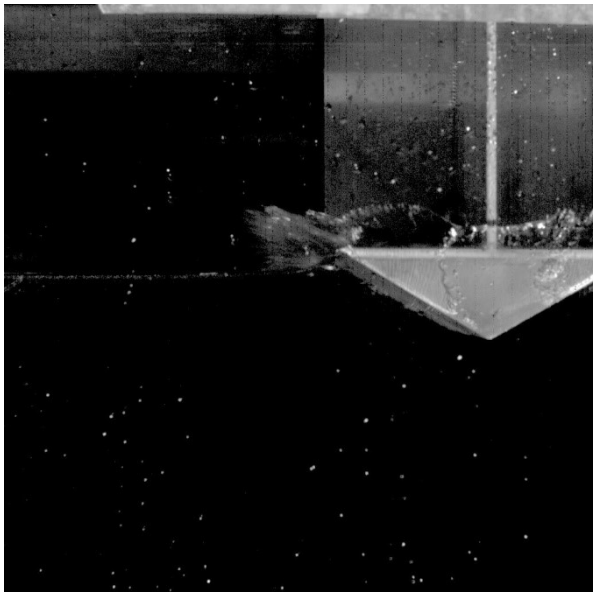

a) at time=0.033s

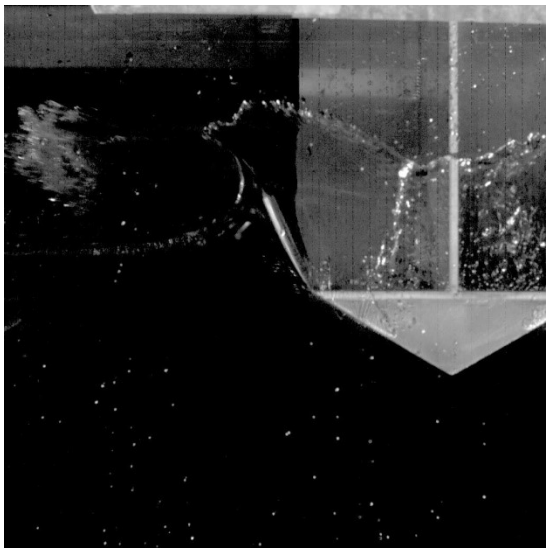

b) at time=0.067s

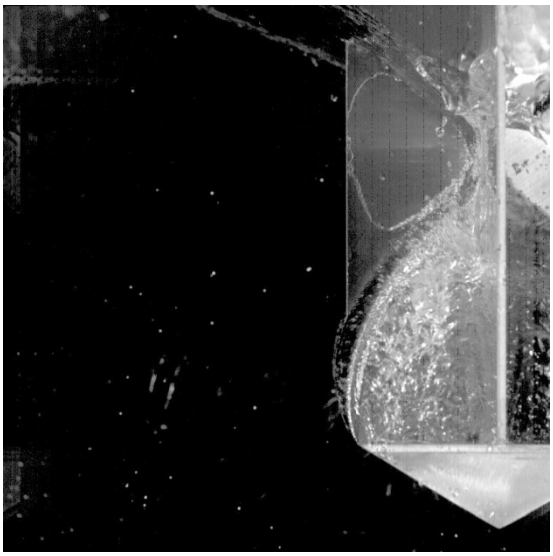

c) at time=0.310s

Fig. 8. Free surface close to the end of the slamming stage, transition stage and collapse stage for test case 2.

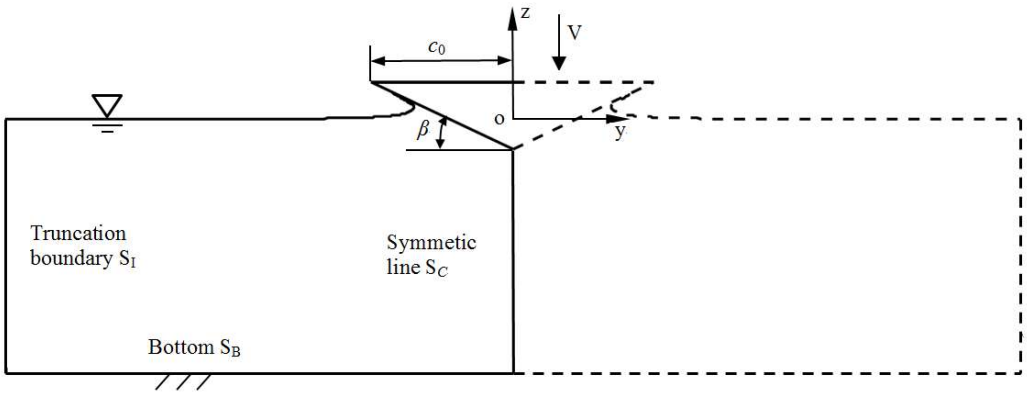

Fig. 9. Coordinate system and symbol definitions used in numerical study of vertical water entry of a 2D wedge.

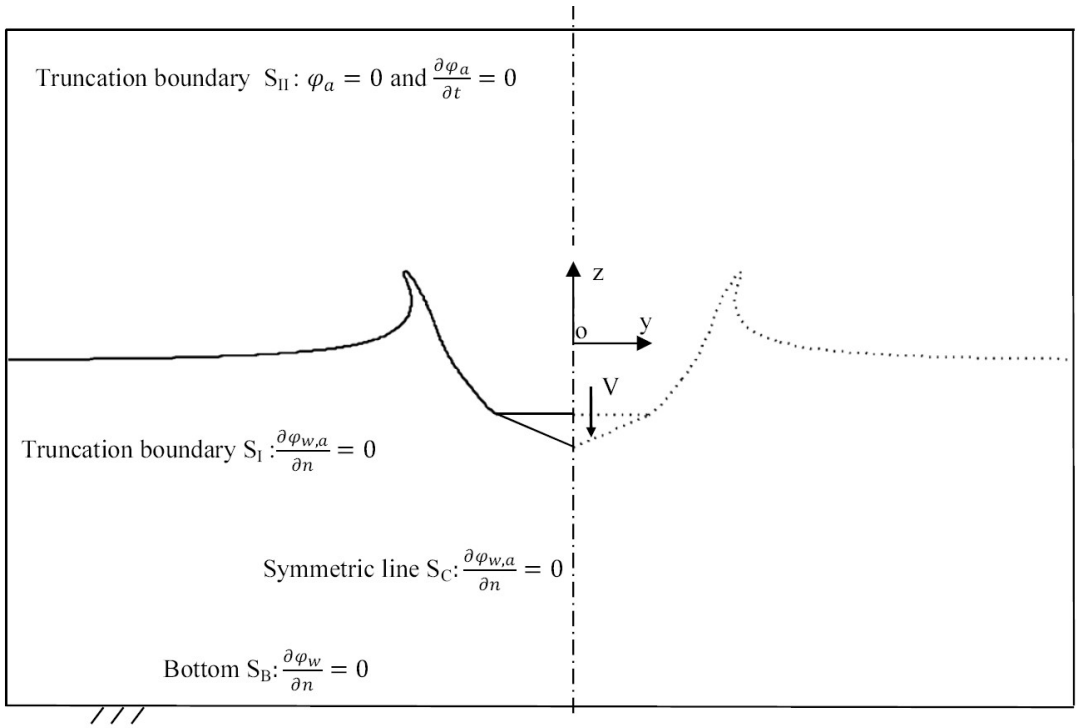

Fig. 10. Coordinate system, symbol definitions and boundary conditions used in numerical study of vertical water entry of a 2D wedge. The dimensionless height of the air region is set to $100c_0$.

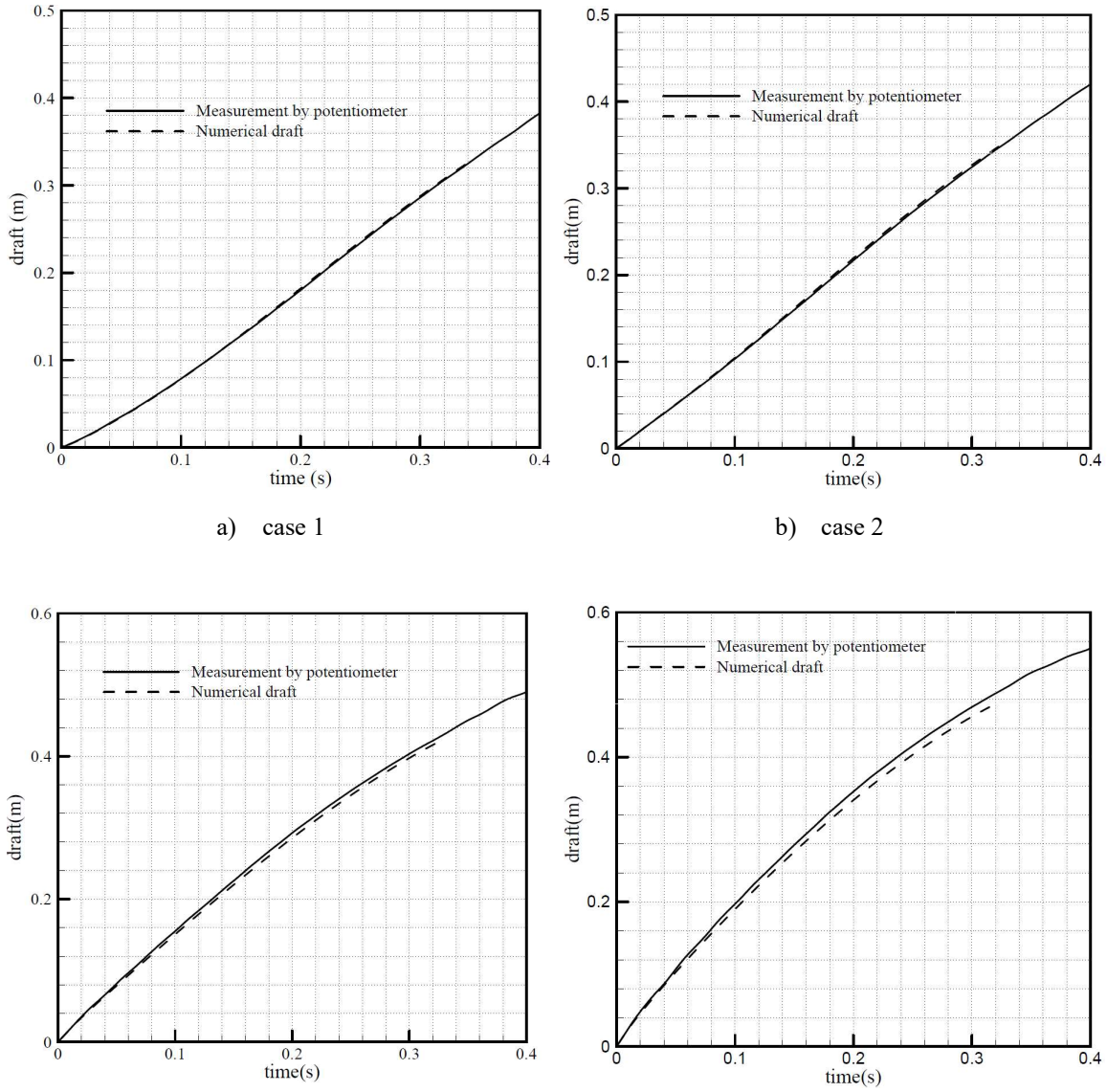

Fig. 11. Comparison of the numerical draft of the wedge and the experimental measurement.

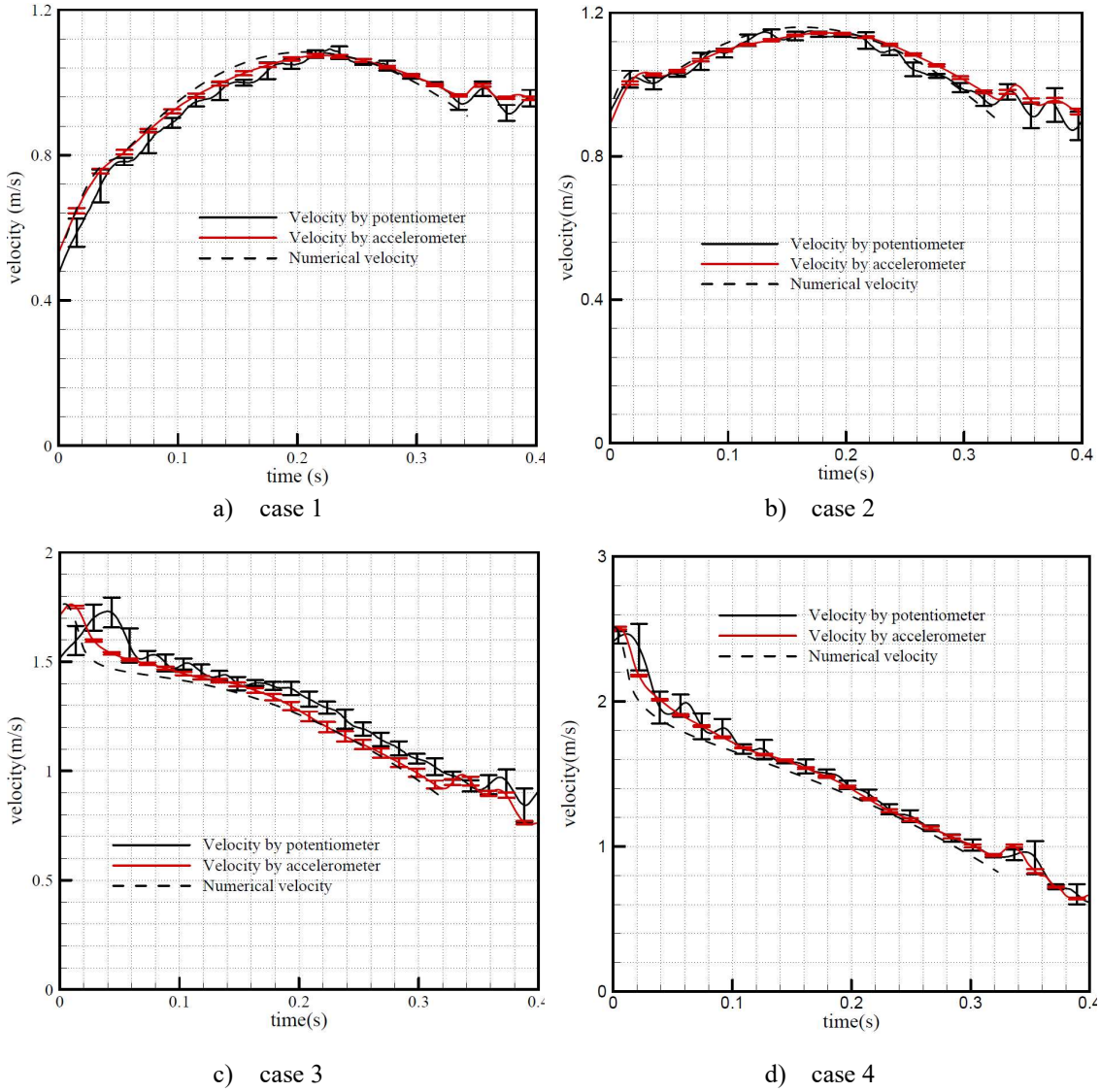

Fig. 12. Comparison of the numerical velocity of the wedge and the experimental measurement.

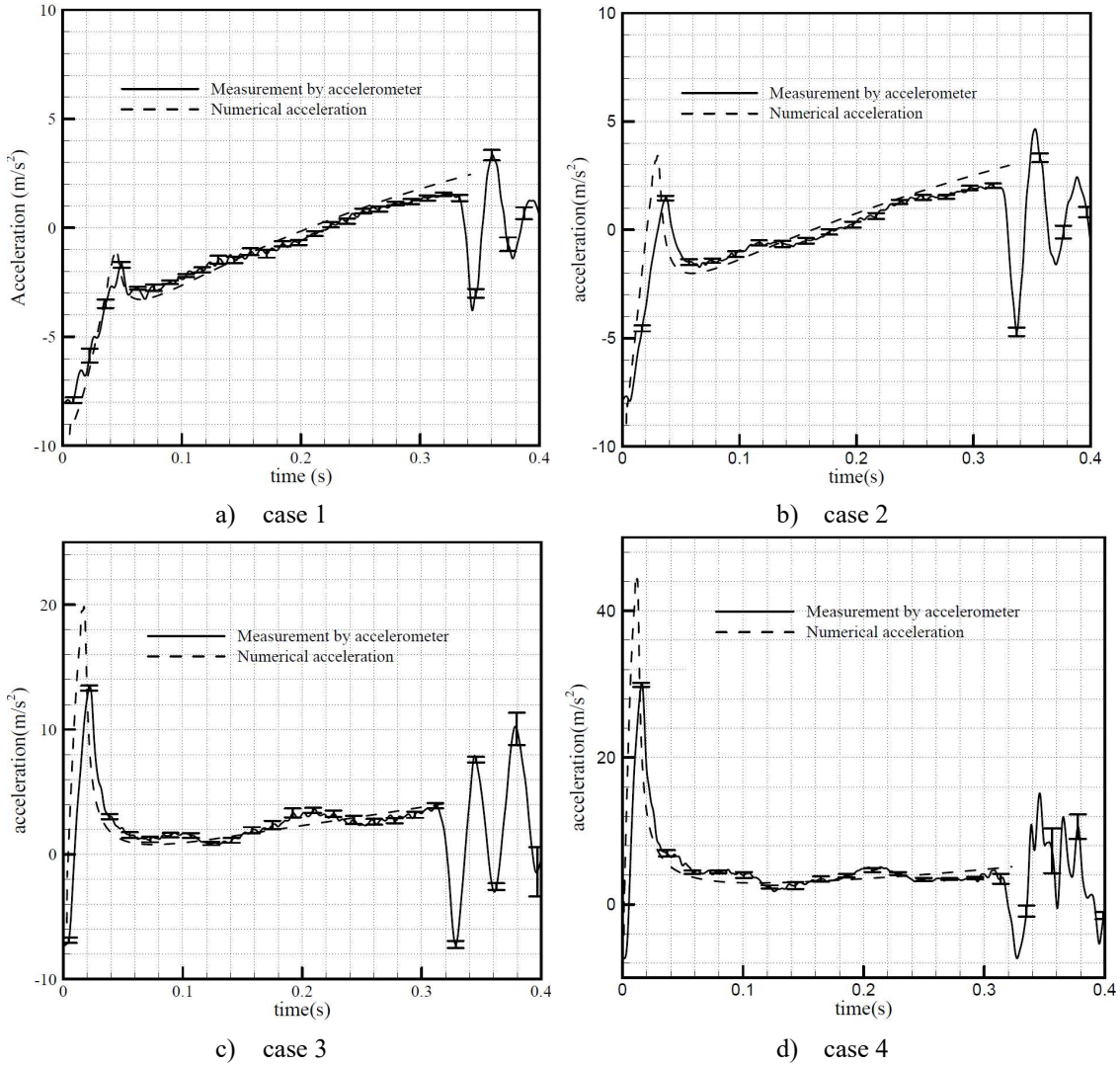

Fig. 13. Comparison of the numerical acceleration of the wedge and the experimental measurement.

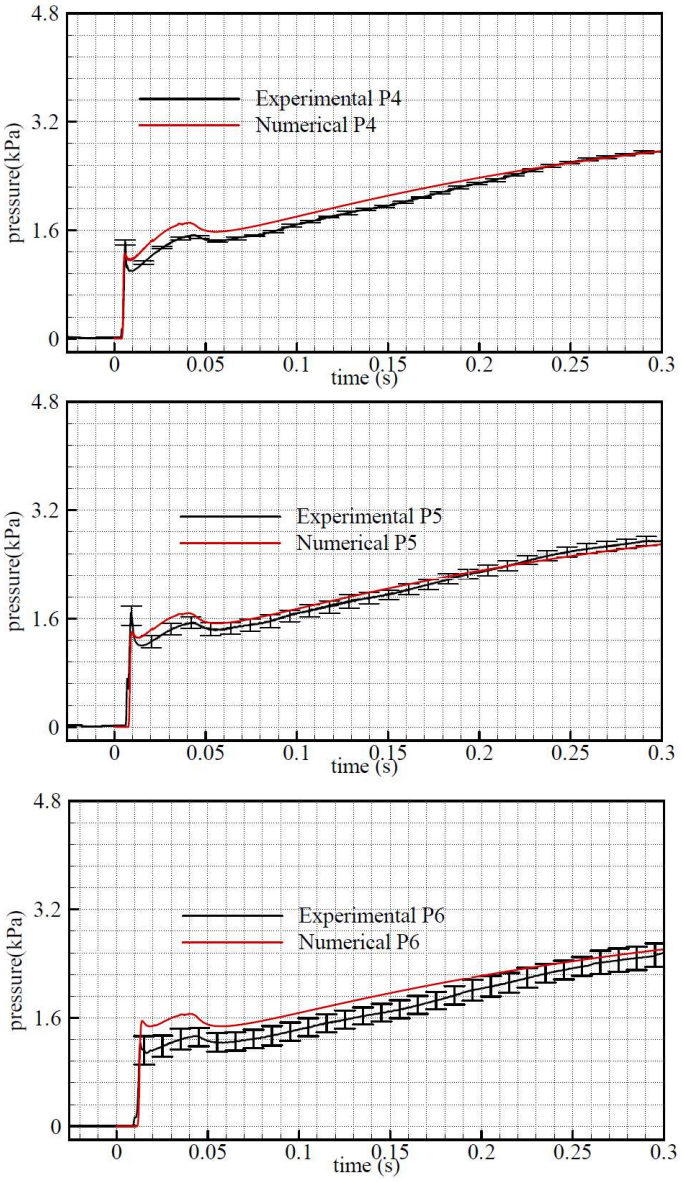

Fig. 14. Time history of P4, P5 and P6 for case 1.

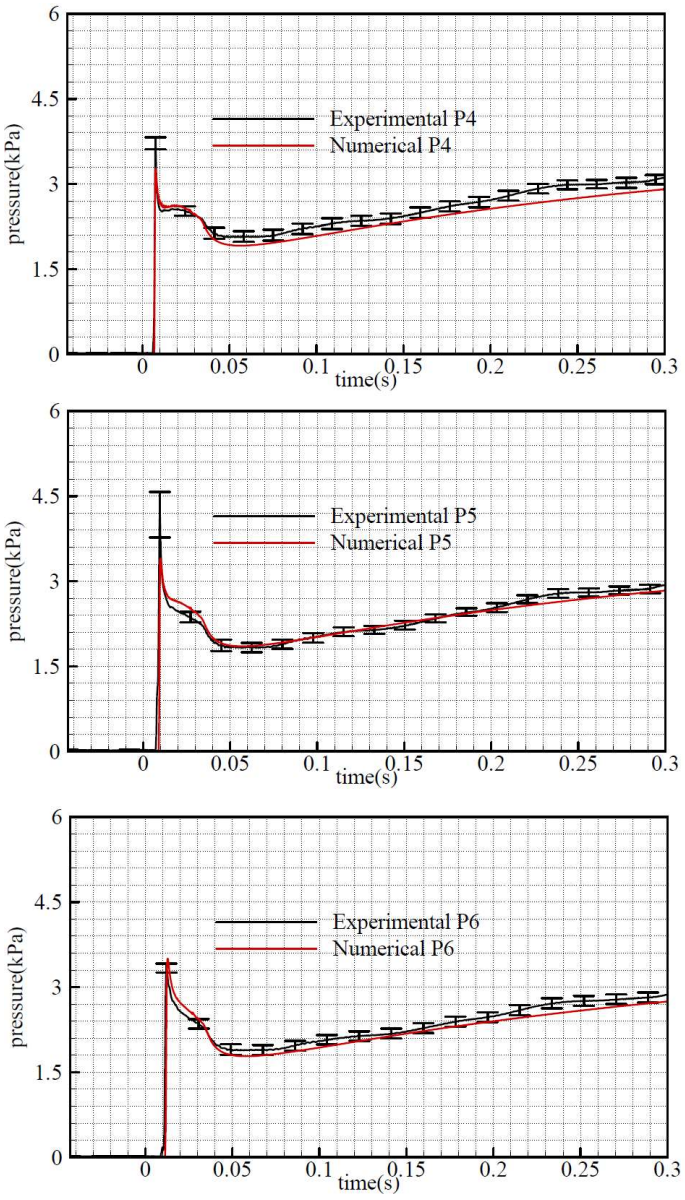

Fig. 15. Time history of P4, P5 and P6 for case 2.

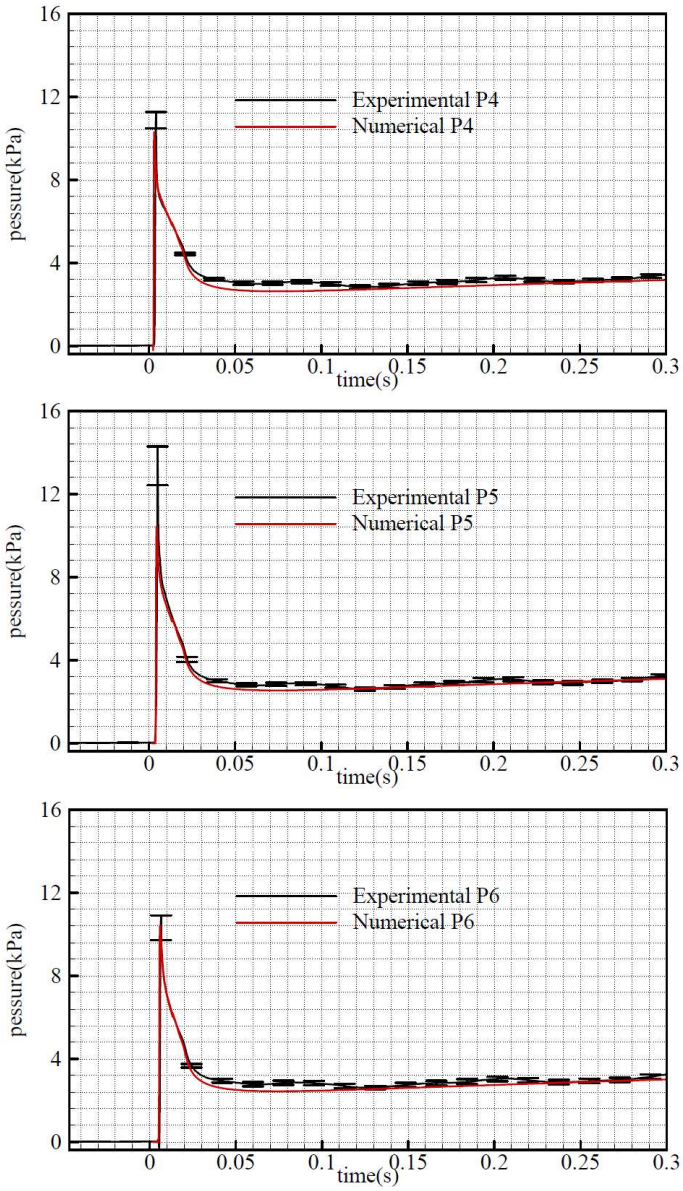

Fig. 16. Time history of P4, P5 and P6 for case 3.

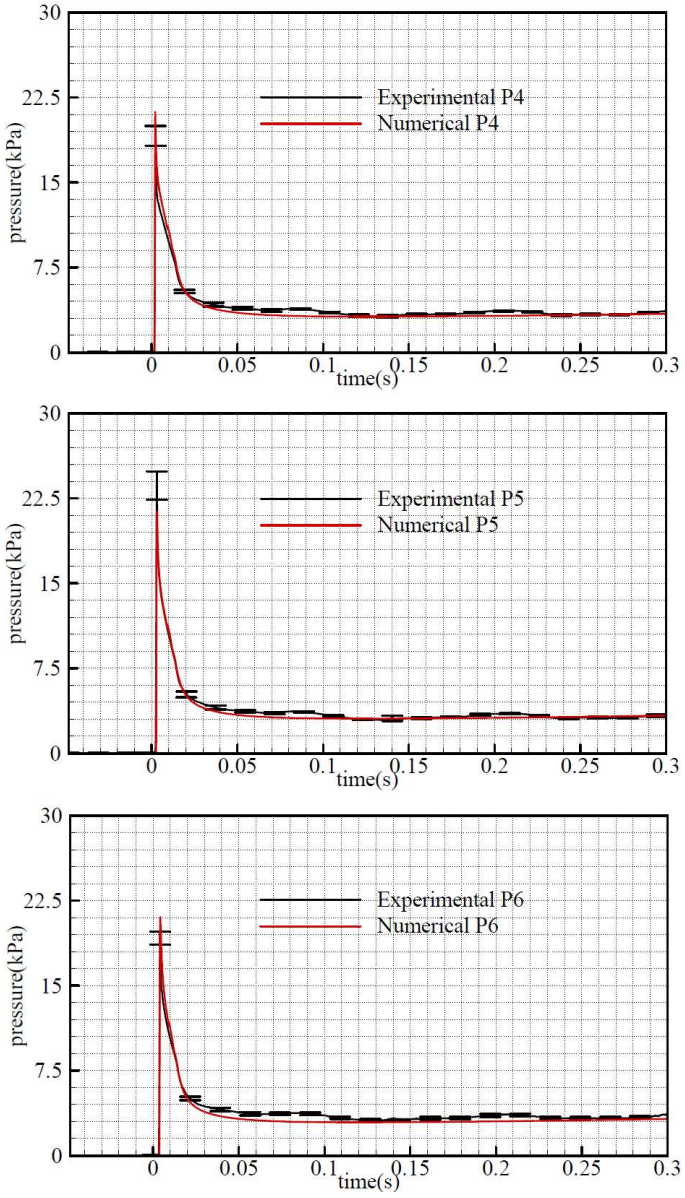

Fig. 17. Time history of P4, P5 and P6 for case 4.

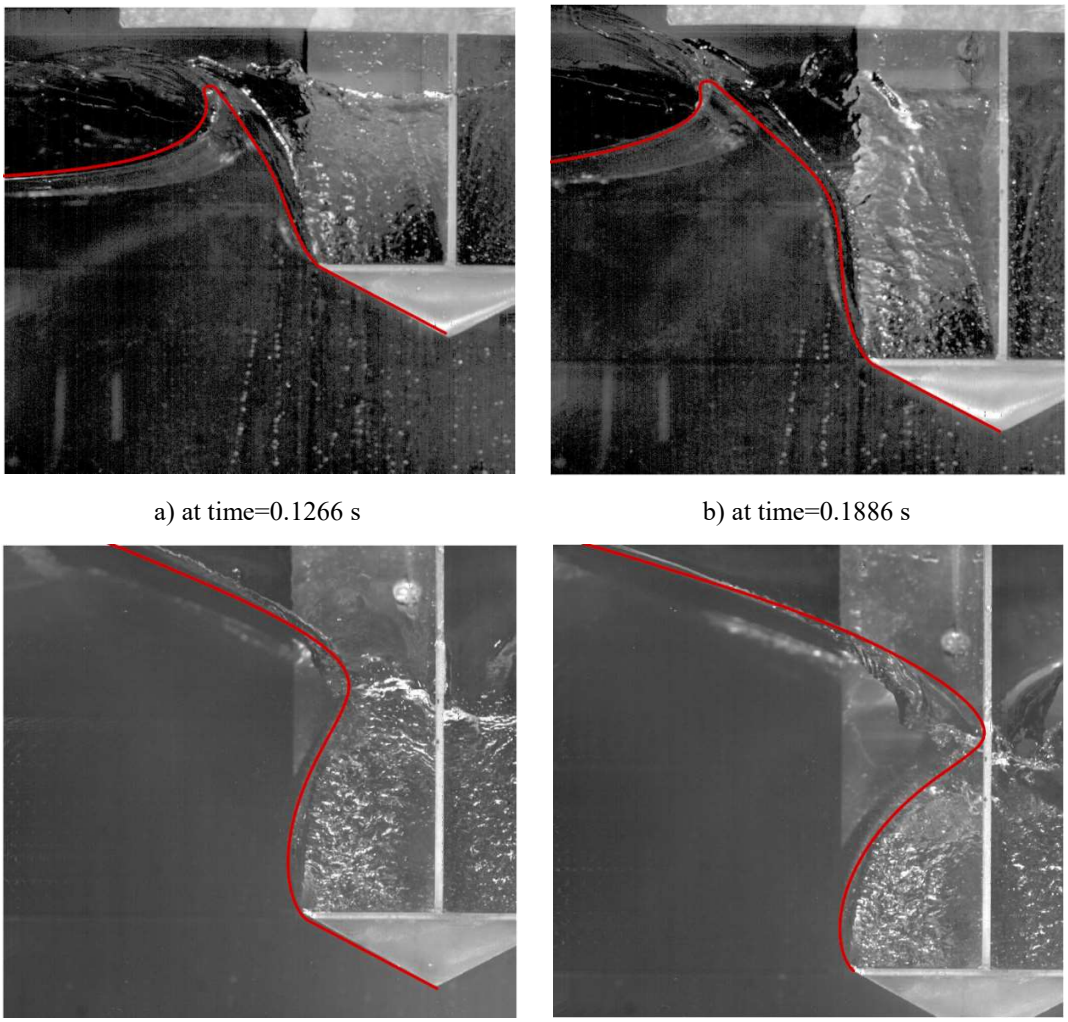

a) at time=0.1266 s

b) at time=0.1886 s

c) at time=0.2871 s

d) at time=0.3422 s

Fig. 18. Comparison of free surface between experimental results and numerical results for case 1. The red solid lines denote the numerical results.

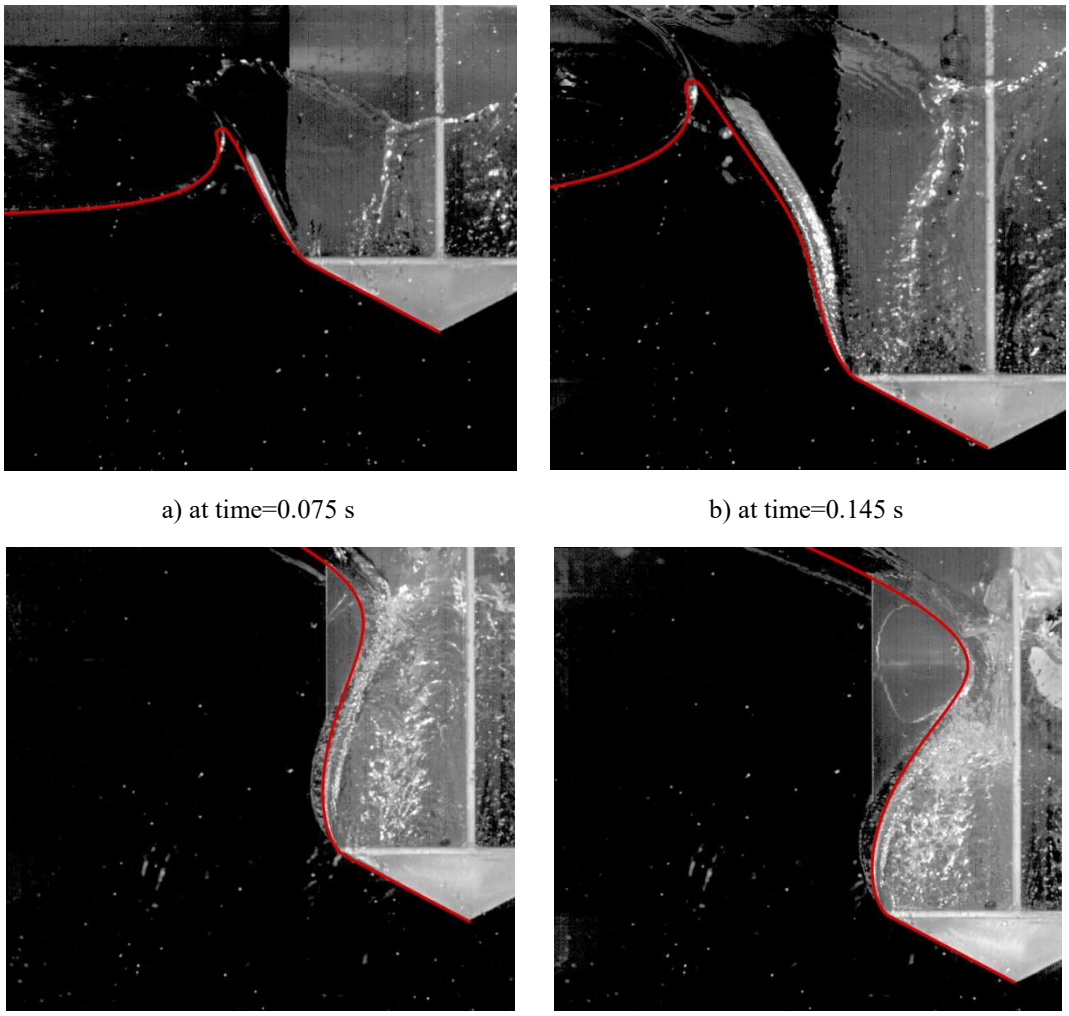

a) at time=0.075 s

b) at time=0.145 s

c) at time=0.262 s

d) at time=0.304 s

Fig. 19. Comparison of free surface between experimental results and numerical results for case 2. The red solid lines denote the numerical results.

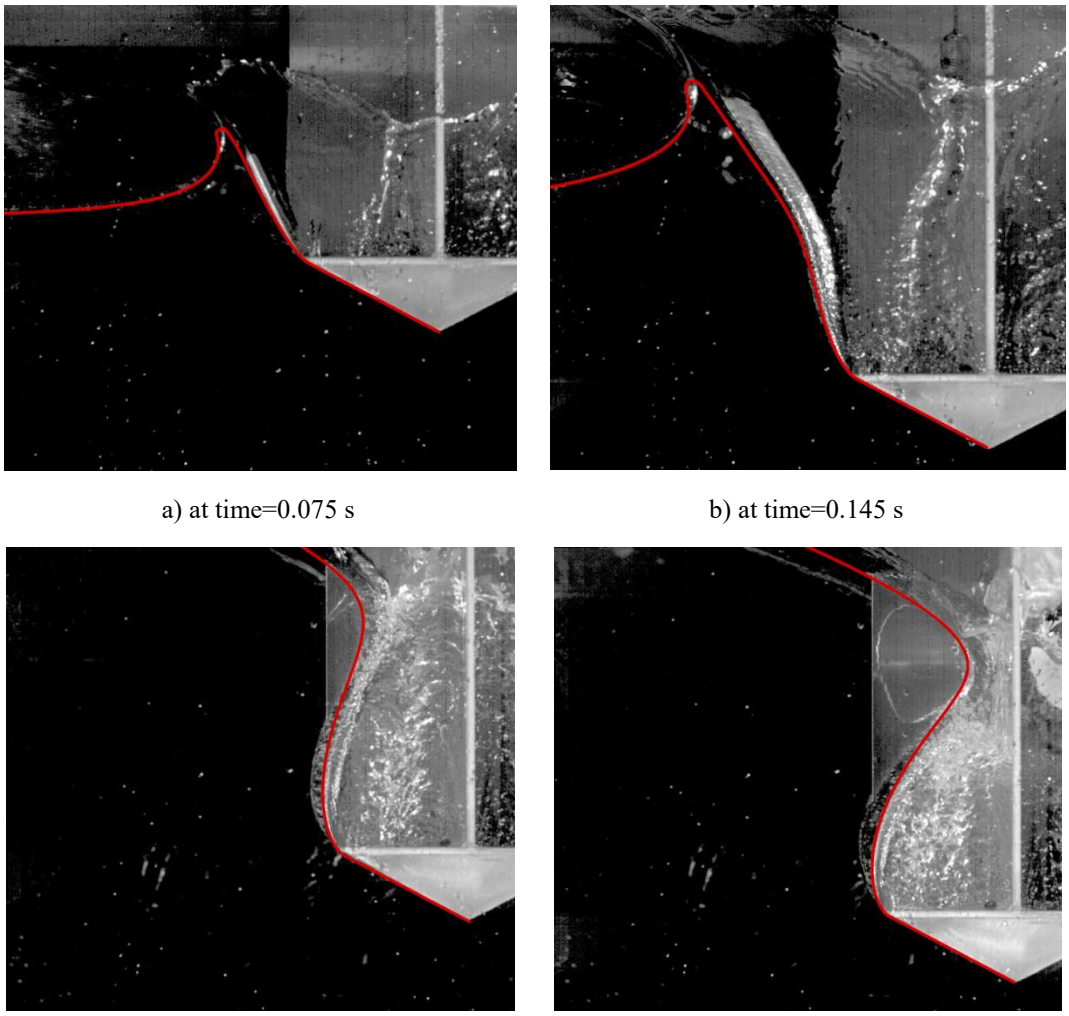

a) at time=0.075 s

b) at time=0.145 s

c) at time=0.262 s

d) at time=0.304 s

Fig. 20. Comparison of free surface between experimental results and numerical results for case 3. The red solid lines denote the numerical results.

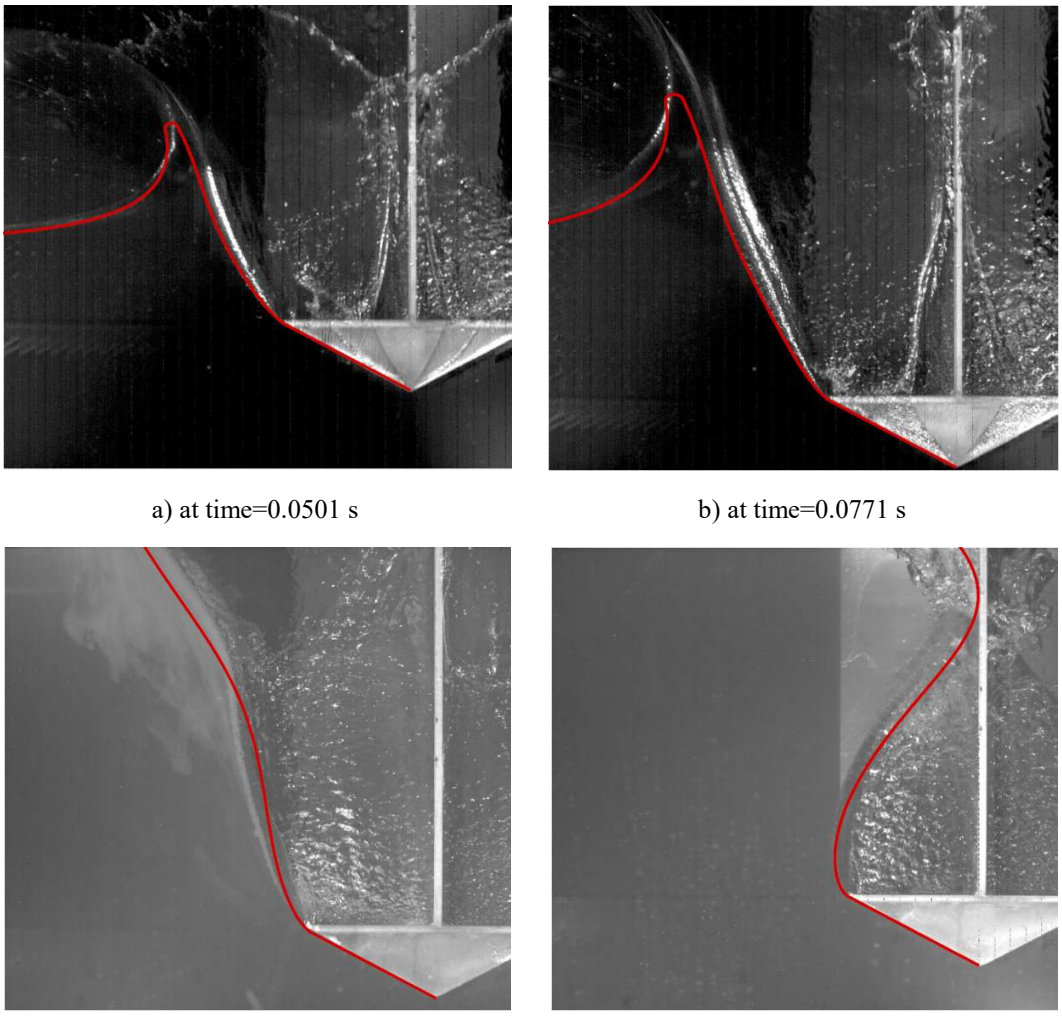

a) at time=0.0501 s

b) at time=0.0771 s

c) at time=0.1741 s

d) at time=0.3223 s

Fig. 21. Comparison of free surface between experimental results and numerical results for case 4. The red solid lines denote the numerical results.

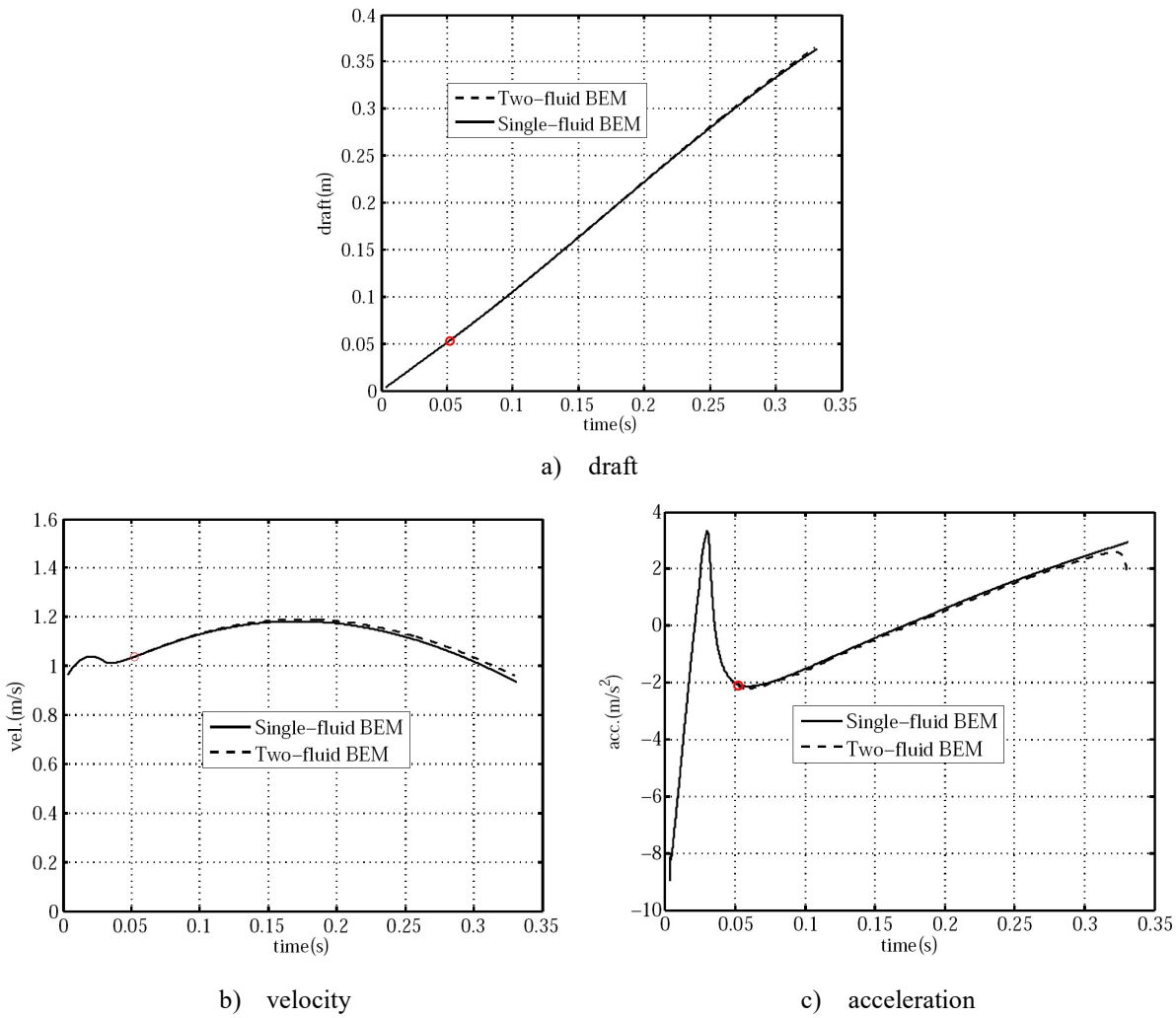

Fig. 22. Numerical results of wedge draft, velocity and acceleration by the single-fluid BEM and two-fluid BEM. The red circle denotes the start of the two-fluid BEM.

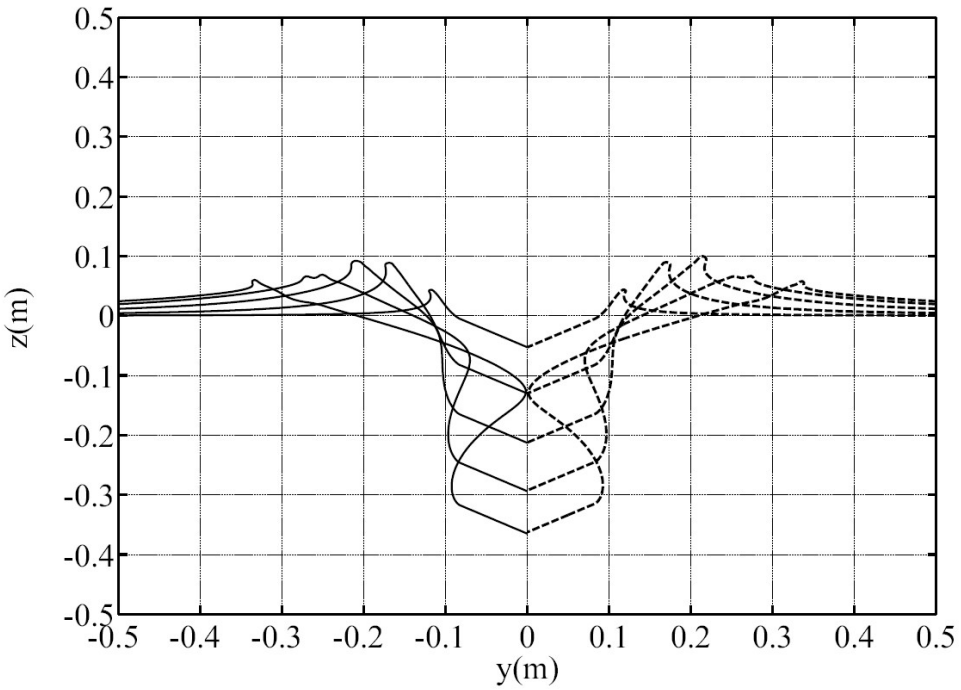

Fig. 23. Comparison of numerical free surface at time t=0.05197, 0.12197, 0.19197, 0.26197 and 0.33017. The solid lines denote the results by two-fluid BEM and the dashed lines the results by single-fluid BEM.

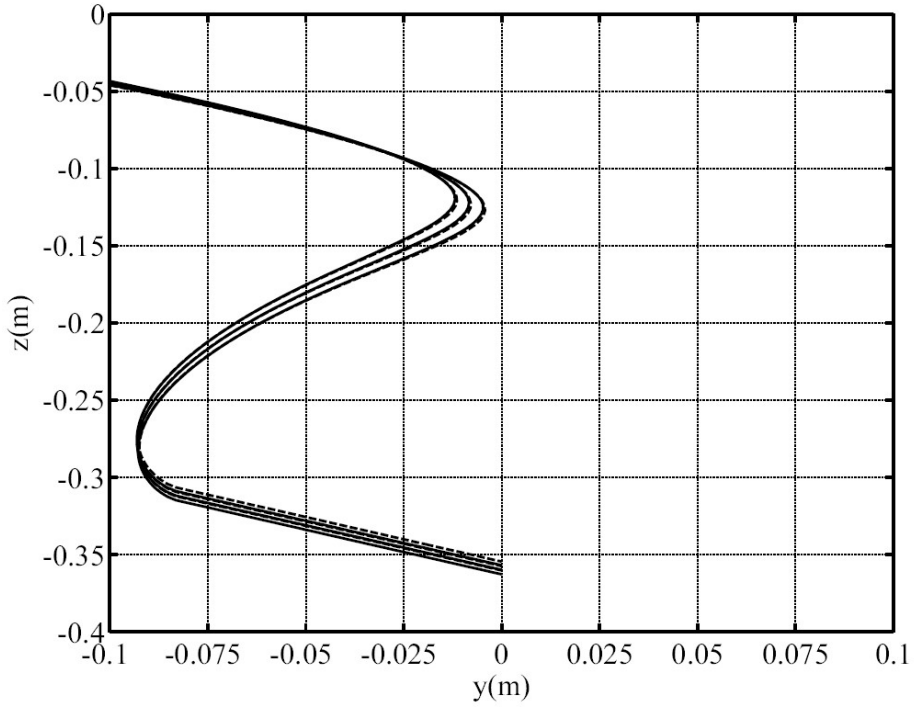

Fig. 24. Comparison of numerical free surface around the cavity at time t=0.32187, 0.32487, 0.32787 and 0.33017. The solid lines denote the results by two-fluid BEM and the dashed lines the results by single-fluid BEM.

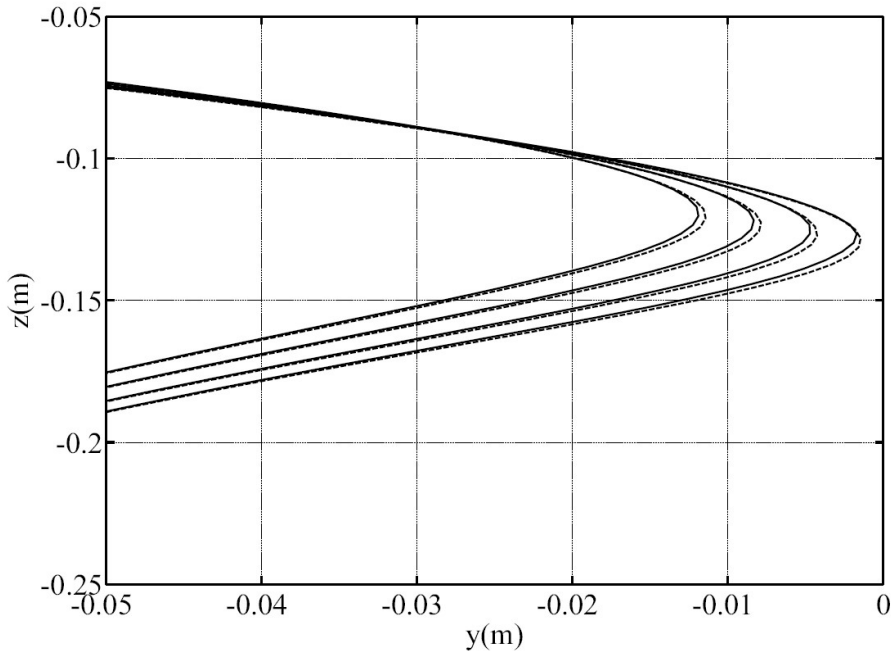

Fig. 25. Comparison of numerical free surface around the pinch-off point at time t=0.32187, 0.32487, 0.32787 and 0.33017. The solid lines denote the results by two-fluid BEM and the dashed lines the results by single-fluid BEM.

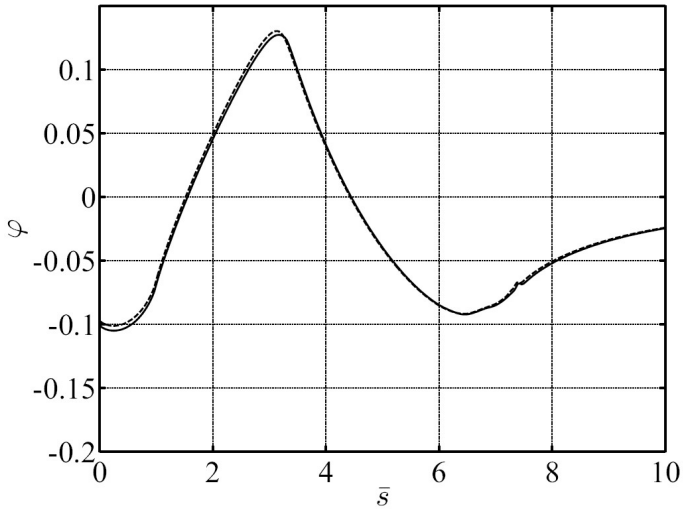

Fig. 26. Comparison of the velocity potential on wedge and free surface at time t=0.33017. $\bar{s} = s * \cos\beta / c_0$, which is measured from the tip of the wedge, represents the non-dimensional arc length of boundary and therefore $\bar{s} = [0\ 1]$ corresponds to the impact side of the wedge. The solid lines denote the results by two-fluid BEM and the dashed lines the results by single-fluid BEM.

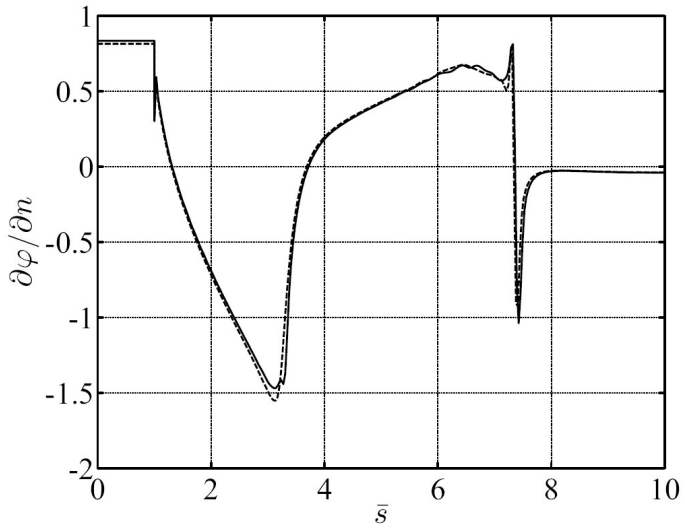

Fig. 27. Comparison of the normal velocity on wedge and free surface at time t=0.33017. $\bar{s} = s * \cos\beta/c_0$, which is measured from the tip of the wedge, represents the non-dimensional arc length of boundary and therefore $\bar{s} = [0\ 1]$ corresponds to the impact side of the wedge. The solid lines denote the results by two-fluid BEM and the dashed lines the results by single-fluid BEM.

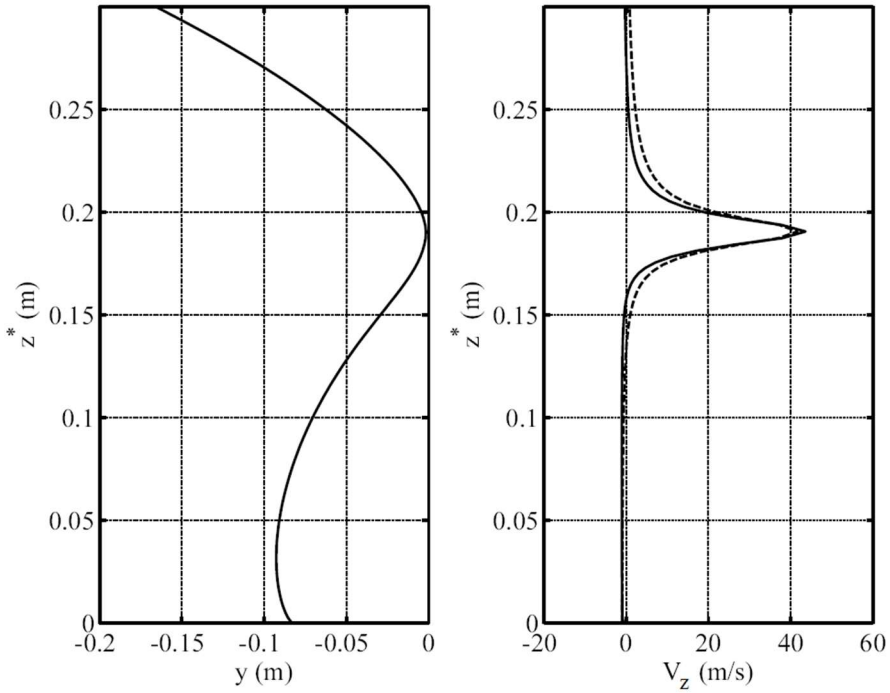

Fig. 28. Numerical predictions of the vertical velocity component of air on the free surface and the symmetrical boundary at time t=0.33017; z^* is the vertical coordinate and measured from the wedge top. In the left subfigure, the solid line represents the numerical free surface; in the right subfigure the solid line represents the vertical velocity component of air on the free surface and the dashed line represents the vertical velocity component of air on the symmetrical boundary.

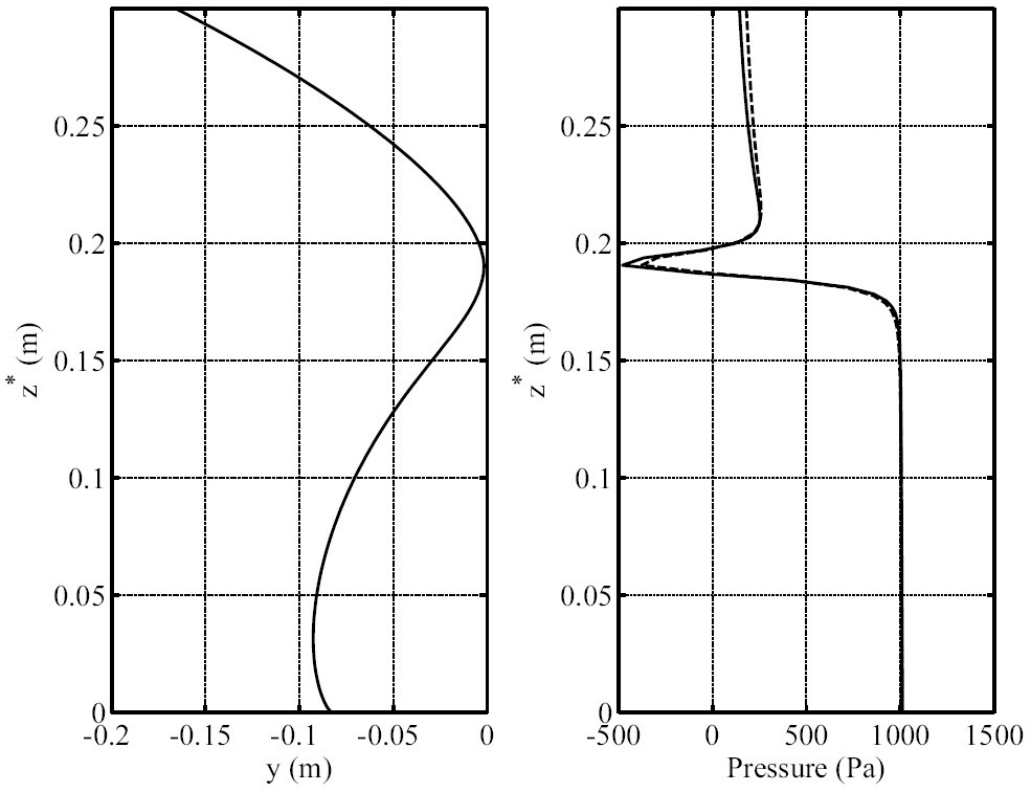

Fig. 29. Numerical predictions of the pressure on the free surface and the symmetrical boundary at time t=0.33017; z^* is the vertical coordinate and measured from the wedge top. In the left subfigure, the solid line represents the numerical free surface; in the right subfigure the solid line represents the pressure on the free surface and the dashed line represents the pressure on the symmetrical boundary.

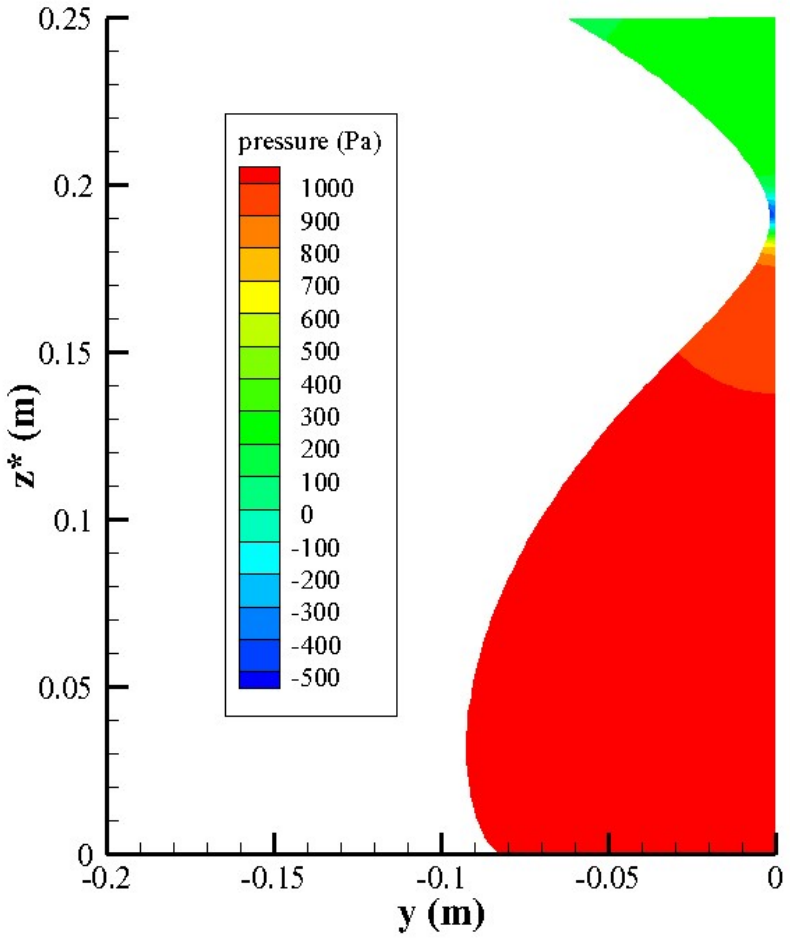

Fig. 30. Numerical predictions of the pressure inside the cavity at time t=0.33017; z^* is the vertical coordinate and measured from the wedge top.

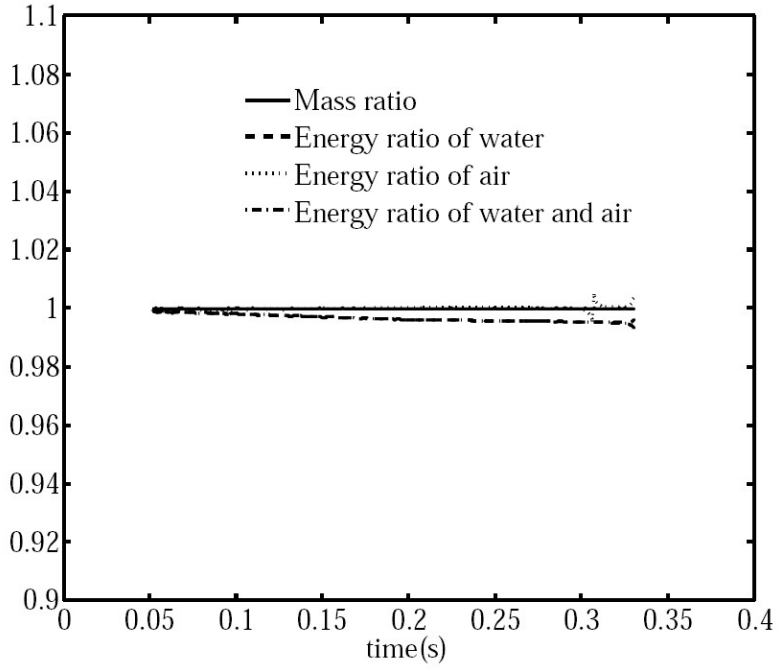

Fig. B1. Check of the conservation of fluid mass and energy for the two-fluid BEM.